Lower Hybrid Experiments on ASDEX in 1989

F.X. Söldner, F. Leuterer and O. Gehre, K. McCormick,
M. Münich, M. Zouhar, Max-Planck-Institut für Plasmaphysik,
EURATOM Association, Garching, Fed. Rep. of Germany

R. Bartiromo, R. De Angelis, L. Gabellieri, V. Pericoli, A. Tuccillo
ENEA , Frascati, Italy

S. Bernabei, T.K. Chu, C. Forest
Princeton Plasma Physics Laboratory, Princeton, USA

R.W. Harvey, General Atomics, San Diego, USA

IPP III / 162 **August 1990**

MAX-PLANCK-INSTITUT FÜR PLASMAPHYSIK

8046 GARCHING BEI MÜNCHEN

MAX-PLANCK-INSTITUT FÜR PLASMAPHYSIK

GARCHING BEI MÜNCHEN

Lower Hybrid Experiments on ASDEX in 1989

F.X. Söldner, F. Leuterer and O. Gehre, K. McCormick,
M. Münich, M. Zouhar, Max-Planck-Institut für Plasmaphysik,
EURATOM Association, Garching, Fed. Rep. of Germany

R. Bartiromo, R. De Angelis, L. Gabellieri, V. Pericoli, A. Tuccillo
ENEA , Frascati, Italy

S. Bernabei, T.K. Chu, C. Forest
Princeton Plasma Physics Laboratory, Princeton, USA

R.W. Harvey, General Atomics, San Diego, USA

IPP III / 162 **August 1990**

Die nachstehende Arbeit wurde im Rahmen des Vertrages zwischen dem Max-Planck-Institut für Plasmaphysik und der Europäischen Atomgemeinschaft über die Zusammenarbeit auf dem Gebiete der Plasmaphysik durchgeführt.

Lower Hybrid Experiments on ASDEX in 1989

F.X.Söldner, F.Leuterer and

O.Gehre, K.McCormick, M. Münich, M.Zouhar

Max-Planck-Institut für Plasmaphysik, EURATOM Association, Garching, Fed. Rep. of Germany

R.Bartiromo, R.De Angelis, L.Gabellieri, V.Pericoli, A.Tuccillo

ENEA , Frascati, Italy

S.Bernabei, T.K.Chu, C.Forest,

Princeton Plasma Physics Laboratory, Princeton, USA

R.W.Harvey

General Atomics, San Diego, USA

Abstract

Lower hybrid experiments were resumed on ASDEX with a system at 2.45 GHz. The full power available from the emitter (2.6 MW) could be routinely transmitted to the plasma. Coupling of the grill antenna was considerably improved after the surrounding protection limiters had been reshaped. Detailed studies of current drive were conducted in ohmic target plasmas and also in combination with NBI. Rather good agreement is found between the experimental results on current drive efficiency and theory. Variations of the current drive efficiency can be closely correlated with variations of the broadening of the lower hybrid pump wave. Improved global energy confinement is obtained with LH at low density. This improvement can be attributed to the superior confinement of the suprathermal electrons. Particle confinement is also improved with LH current drive. The MHD activity is strongly influenced by LH current drive. Sawteeth can be suppressed in OH- and NBI-heated discharges with LH current drive. Stabilization of the m=1 mode is achieved with LH current drive at low $N_{||}$, in OH target plasmas and also in combination with NBI. After suppression of the m=1 mode strong central electron heating and peaking of the radial electron temperature profile are obtained. The current profile j(r) can be controlled by varying the LH spectrum. Current and temperature profiles can thus be decoupled and all MHD modes be simultaneously suppressed by LH current drive.

The Lower Hybrid experiments are performed in collaboration between IPP Garching, ENEA Frascati and PPPL Princeton.

Table of contents

1. Technical layout of the rf system

Lower Hybrid waves are injected into ASDEX in the actual experiments at 2.45 GHz with nominal power of 3 MW and maximum pulse duration of 1 s /1/.

The transmitter consists of 6 klystron amplifiers (Varian VKS-8296 A) with an output power of 500 kW each. Without extension of the cooling facilities the pulse length is restricted to 1 s. Each klystron is protected against excessive reflected power by means of a four-port circulator (insertion loss 0.4 dB) which can be operated into a VSWR = 6 for 1 s and into VSWR = ∞ for 0.1 s. The remaining reflection back into the klystron is < -20 dB for any phase of a short circuit at the output of the circulator. The klystrons are arranged in two groups of three tubes (Fig.1). Each group is fed by one high-voltage power supply (0 - 70 kV/50 A) and protected by two parallel ignitron crowbar systems. These crowbars trigger in the event of arcing in one of the tubes (dI_b/dt), too high a beam voltage or too high a body current. Its response time is < 5 µs. The control system of the transmitter is the same as used in the previous 1.3 GHz experiment. The klystrons were previously used on the FT tokamak in Frascati and on the PLT tokamak in Princeton. In the actual configuration on ASDEX they are fed from one common master oscillator (1 W) through six solid-state intermediate amplifiers (5 W). The amplitude and phase in each line are feedback-controlled within a range of 20 dB (±0.1 dB) and 360° (±2°), respectively, with a combined characteristic time of 2 ms. The amplitude control can be used for calibrated modulation of the output power.

Six transmission lines of standard WR 430 waveguides connect the klystrons to a power splitter system where the power of each klystron is divided into eight channels. The power division is performed by successive stages of 3 dB-E plane hybrids which are terminated on arm 4 with dry loads (125 W/l s). Their directivity is better than 30 dB and a short circuit in any one of the output waveguides affects the forward power in any other waveguide by < 0.5 dB. In each of the 48 outputs of the power splitter system the phase can be varied through 360° (±2.5°), resulting in a high degree of experimental flexibility with respect to the wave spectrum. These phase shifters are driven by a step motor, and a variety of phase settings stored in a personal computer can be loaded by remote control between successive ASDEX shots.

The 48 output waveguides are then connected through step transformers, DC-breaks and a structure of bent narrow waveguides (10 x 109 mm) to the input of a 2 x 24 waveguide grill antenna. This antenna includes two blocks with 24 ceramic waveguide windows each. Two stainless steel front ends finally touch the plasma boundary a few millimetres behind the protection limiter radius. The inner surfaces of the front ends are coated with a rough gold layer

to reduce the risk of multipactor breakdown in the waveguides. Arc detectors, sidewall directional couplers and a VSWR measurement in each of the grill waveguides allow fast tripping of the RF power in the event of arcing (1 μs) or excessive reflection (100 μs) in any one of the 48 waveguides.

Each row of 24 waveguides of the grill is connected to one of the two groups of klystrons. They can thus be operated independently with respect to time, pulse length, power and wave spectrum. The signals recorded in the data acquisition system include the 6 input powers into the power splitter and their phases, 48 grill input powers and 48 grill reflection powers. The grill input phases are recorded through a time multiplex system, allowing all 48 channels to be sampled twice during a 1 s pulse.

The system was put into operation on Dec. 15, 1988. After a total of 80 shots with different phase settings and varying plasma conditions a power level of 1 MW for 0.5 s was achieved.

This new lower hybrid system was constructed in cooperation between ENEA Frascati (grill antenna,bent waveguide structures, 3 klystrons, socket tanks, transmission line), PPPL Princeton (waveguide windows, 3 klystrons) and IPP Garching (ASDEX interface, power splitter, transmitter, low-power system, control system, data acquisition).

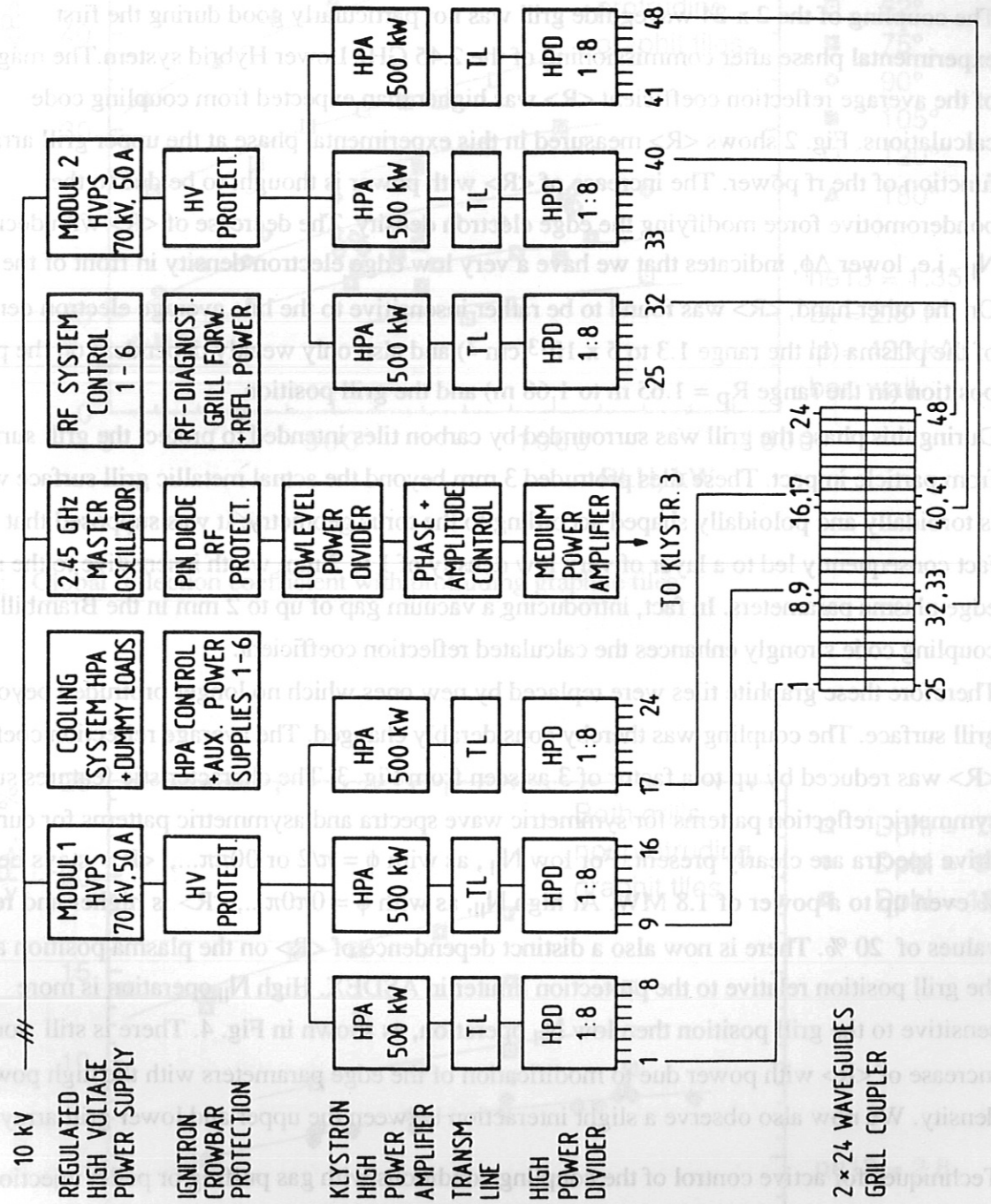

Fig. 1: Block diagram of the 2.45 GHz Lower Hybrid system on ASDEX.

2. *Coupling*

The coupling of the 2 x 24 waveguide grill was not particularly good during the first experimental phase after commissioning of the 2.45 GHz Lower Hybrid system.The magnitude of the average reflection coefficient <R> was higher than expected from coupling code calculations. Fig. 2 shows <R> measured in this experimental phase at the upper grill array as a function of the rf power. The increase of <R> with power is thought to be due to the ponderomotive force modifying the edge electron density. The decrease of <R> with decreasing $N_{||}$, i.e. lower $\Delta\phi$, indicates that we have a very low edge electron density in front of the grill. On the other hand, <R> was found to be rather insensitive to the line average electron density $\bar{n}_e$ of the plasma (in the range 1.3 to 5 x 10^{13} cm^{-3}) and also only weakly dependent on the plasma position (in the range R_p = 1.65 m to 1.68 m) and the grill position.

During this phase the grill was surrounded by carbon tiles intended to protect the grill surface from particle impact. These tiles protruded 3 mm beyond the actual metallic grill surface which is toroidally and poloidally shaped according to the torus geometry. It was supposed that this fact consequently led to a layer of very low density of 1 to 2 mm width insensitive to the main edge plasma parameters. In fact, introducing a vacuum gap of up to 2 mm in the Brambilla coupling code strongly enhances the calculated reflection coefficient.

Therefore these graphite tiles were replaced by new ones which no longer protruded beyond the grill surface. The coupling was thereby considerably changed. The average reflection coefficient <R> was reduced by up to a factor of 3 as seen from Fig. 3. The characteristic features such as symmetric reflection patterns for symmetric wave spectra and asymmetric patterns for current drive spectra are clearly present. For low $N_{||}$, as with $\phi = \pi/2$ or $00\pi\pi...$, <R> stays below 10 % even up to a power of 1.8 MW. At high $N_{||}$, as with $\phi = 0\pi0\pi...$, <R> is higher and reaches values of 20 %. There is now also a distinct dependence of <R> on the plasma position and on the grill position relative to the protection limiter in ASDEX. High $N_{||}$ operation is more sensitive to the grill position then low $N_{||}$ operation, as shown in Fig. 4. There is still some increase of <R> with power due to modification of the edge parameters with the high power density. We now also observe a slight interaction between the upper and lower grill arrays.

Techniques for active control of the coupling conditions with gas puffing or pellet injection have been tested recently /2/.

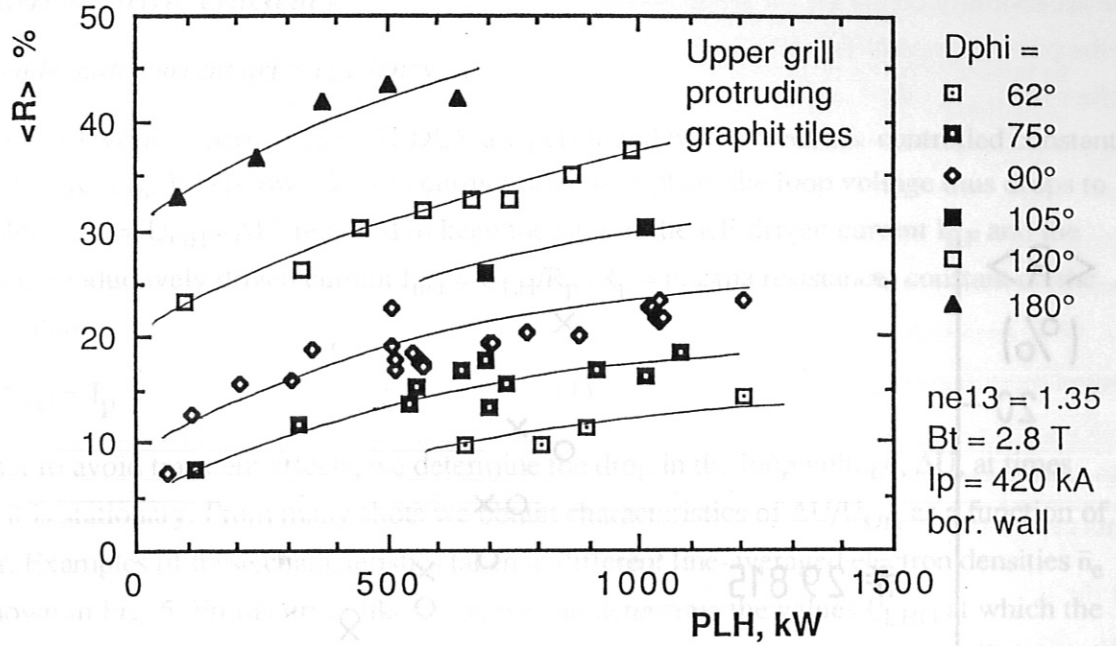

Fig. 2: Global reflection coefficient with protruding graphite tiles.

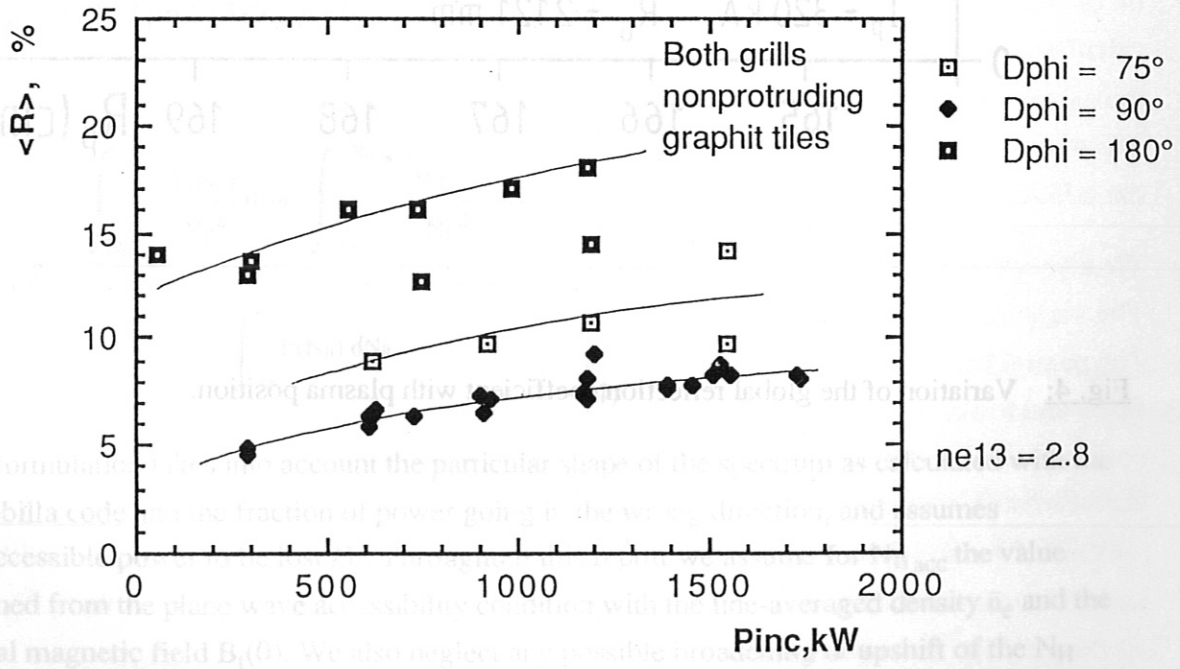

Fig. 3: Global reflection coefficient with nonprotruding graphit tiles.

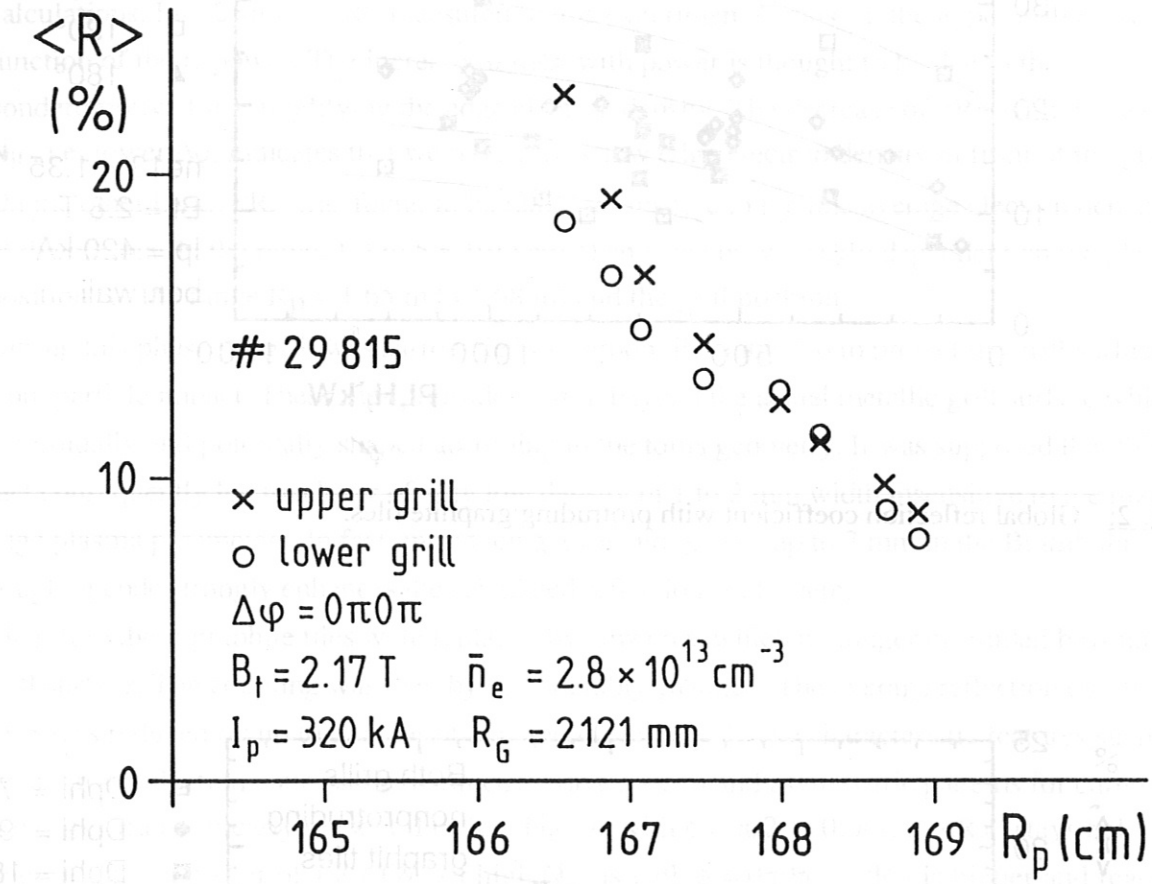

Fig. 4: Variation of the global reflection coefficient with plasma position.

3. *Current drive efficiency*

3.1 Steady-state current drive efficiency

The Lower Hybrid experiments in ASDEX are performed with a feedback-controlled constant plasma current I_p. When lower hybrid current drive is applied, the loop voltage thus drops to the value $U_{LH} = U_{OH} - \Delta U$, required to keep the sum of the RF-driven current I_{RF} and the remaining inductively driven current $I_{ind} = U_{LH}/R_p$ (R_p = plasma resistance) constant on the preset value:

$$I_{RF} + I_{ind} = I_p. \qquad (1)$$

In order to avoid transient effects, we determine the drop in the loop voltage, ΔU, at times when it is stationary. From many shots we obtain characteristics of $\Delta U/U_{OH}$ as a function of power. Examples of these characteristics taken at different line-averaged electron densities $\bar{n}_e$ are shown in Fig. 5. From curves like these, we can determine the values P_{LHO} at which the loop voltage is zero, i.e. $\Delta U = U_{OH}$. The experimental steady-state current drive efficiency is then

$$\eta_{o,exp} = I_p \, \bar{n}_e \, R \, / \, P_{LHO} \, , \qquad (2)$$

where R is the major radius of the plasma. On the assumption of homogeneous current density and power deposition profiles, j(r) and p(r), we can derive from theory

$$\eta_{o,theor} = 1240 \, / \, [\ln\Lambda \, (5+Z_{eff}) \, \langle N_{||}^2 \rangle] \, , \qquad (3)$$

with

$$1 \, / \, \langle N_{||} \rangle^2 = \frac{\displaystyle\int_{N_{||\,acc}}^{\infty} \frac{P(N_{||})}{N_{||}^2} \, dN_{||} - \int_{-\infty}^{-N_{||\,acc}} \frac{P(N_{||})}{N_{||}^2} \, dN_{||}}{\displaystyle\int_{-\infty}^{\infty} P(N_{||}) \, dN_{||}} \, . \qquad (4)$$

This formulation takes into account the particular shape of the spectrum as calculated with the Brambilla code and the fraction of power going in the wrong direction, and assumes nonaccessible power to be lost /3/. Throughout this report we assume for $N_{||\,acc}$ the value obtained from the plane wave accessibility condition with the line-averaged density $\bar{n}_e$ and the central magnetic field $B_t(0)$. We also neglect any possible broadening or upshift of the $N_{||}$ spectrum due to toroidal or nonlinear effects.

In Fig. 6 we plot $\eta_{o,theor}$ as a function of the grill phasing for three different values of $N_{||\,acc}$ and $Z_{eff} = 5$ (solid lines), and for $N_{||\,acc} = 1.5$ and different Z_{eff} (dashed lines). According to

the accessibility condition for plane waves in a homogeneous plasma, $N_{\parallel acc} = 1.5$ corresponds to the parameter combination $\bar{n}_e = 1.4 \cdot 10^{13}$ cm^{-3} and $B_t = 2.8$ T. Also shown in Fig. 2 are the values of $\eta_{o,exp}$ taken in plasmas with a line-averaged density of $\bar{n}_e = 1.35 \cdot 10^{13}$ cm^{-3} and a magnetic field of $B_t = 2.8$ T. For the different machine wall conditions, namely bare stainless-steel walls, carbonized walls, or boronized walls, the values for Z_{eff} as determined from bremsstrahlung are between 3 and 7. The point for $\Delta\varphi = 120^o$ is given in brackets since for this phasing we did not really reach zero loop voltage and P_{LHO} was determined by extrapolation. For these parameters only the case for $\Delta\varphi = 67^o$ suffers in respect of accessibility. At all other phases the full spectrum is accessible. In spite of the assumptions underlying the model we find pretty good agreement with the theory in this low-density case. At higher densities, but with still fully accessible spectrum, the experimentally observed efficiency is less than calculated. This can be correlated to nonlinear effects as described in chapter 4.

At the low density, $\bar{n}_e = 1.35 \cdot 10^{13}$ cm^{-3}, we also combined lower hybrid current drive at low $N_\parallel$, $\Delta\varphi = 90^o$, launched with one grill, with a small amount of power (≈160 kW) launched at high $N_\parallel$, $\Delta\varphi = 180^o$, with the other grill. As compared with current drive with low $N_\parallel$ alone, this leads to a strong decrease of the internal inductance, indicating a shifted power deposition profile radially outward. Nevertheless we need about the same current drive power at low $N_\parallel$ to achieve zero loop voltage, i.e. we have the same overall current drive efficiency.

At higher densities changes in accessibility have to be taken into account. The dependence of η_o on the density is shown in Fig. 7 for plasmas with $B_t = 2.8$ T. The theoretical curves are calculated for $Z_{eff} = 5$, while the experimental values for Z_{eff} vary between 3 and 7. Although the agreement between theory and experiment is not as good as in Fig. 6, we still recognize the importance of accessibility particularly in the density region around $\bar{n}_e = 2 \cdot 10^{13}$ cm^{-3}, where the efficiencies of the $\Delta\varphi = 75^o$ and the $\Delta\varphi = 90^o$ spectra become equal.

We also applied lower hybrid current drive to neutral-beam-heated plasmas in the L-mode. The variation of the loop voltage as a function of the lower hybrid power is shown in Fig. 8. The neutral beam power was kept constant at ≈1 MW in co-injection. During combined neutral beam and lower hybrid injection we get a density increase from 2.1 to $2.4 \cdot 10^{13}$ cm^{-3}. For comparison with current drive in an ohmic plasma we see in Fig. 8 as dashed lines the characteristics obtained at $\bar{n}_e = 2.1 \cdot 10^{13}$ cm^{-3} and $\bar{n}_e = 2.8 \cdot 10^{13}$ cm^{-3}. From this it is concluded that the current drive efficiency at zero electric field is essentially the same without and with neutral beam heating. The zero loop voltage point with neutral injection from Fig. 8 is marked in Fig. 7 as a thick cross.

3.2 *Current drive with non-zero electric field*

When a DC electric field E is present, the fast current-carrying electrons are accelerated or decelerated, depending upon the sign of E. As a consequence, the current drive efficiency changes as described in a number of papers. For comparison of our experimental results with theory we adopt the analytic approximation by K. Yoshioka et al. /4/, who calculated the current drive efficiency η with electric field, normalized to the efficiency η_o without electric field, as

$$\eta / \eta_o = \ln [(1-x_2) / (1-x_1)] / (x_1-x_2) \qquad (5)$$

with $\eta_o = j / p$, $x_{1,2} = \alpha (u_{1,2})^2 E_N$, $\alpha = 12 / (Z_{eff} + 7)$, $u = v_{ph} / v_{th}$, and $E_N = E / E_{Dreicer}$. The indices 1 and 2 relate to the lower and upper boundaries of the effective phase velocity spectrum.

Again assuming homogeneous profiles and combining eq. (5), eq.(1) and the circuit equation $U_{LH} = I_{ind} \cdot R_p$, we obtain

$$P_{LH} / P_{LHO} = (1 - U_{LH} / U_{OH} \cdot T) / \eta / \eta_o \qquad (6)$$

Here the factor T describes the variation of the plasma resistance R_p due to bulk electron heating and a change in Z_{eff} during the application of RF power. Using Spitzer resistivity, we get for T:

$$T = R_{p,OH} / R_{p,LH} \qquad (7)$$

$$= (Z_{eff,OH} + 0.72) / (Z_{eff,LH} + 0.72) \cdot (T_{e,LH} / T_{e,OH})^{3/2}.$$

The term $x_2 \sim E$ in eq. (5) can be expressed as

$$x_2 = U_{LH} / U_{OH} \cdot A \,, \qquad (8)$$

with

$$A = 0.023 \, (Z_{eff,OH} + 0.72) / (Z_{eff,LH} + 7) \cdot I_p / \bar{n}_e \, (N_{||2})^2 \, T_{e,OH}^{3/2} \,, \qquad (9)$$

where I_p , $\bar{n}_e$, T_e are in units kA, 10^{13} cm^{-3}, keV. A is seen to depend on the density $\bar{n}_e$, the total plasma current I_p, the electron temperature $T_{e,OH}$ in the OH phase, Z_{eff}, and the high phase velocity limit $N_{||2}$ of the $N_{||}$ spectrum, which is eventually given by accessibility. Except for $N_{||2}$ all these quantities can be determined experimentally.

In Fig. 9 we compare measurements taken at two different densities, $\bar{n}_e = 1.35 \cdot 10^{13}$ cm^{-3} and $\bar{n}_e = 2.8 \cdot 10^{13}$ cm^{-3}, with this theory. From the measured values of the volume-averaged Z_{eff}, the volume-averaged $T_{e,OH}$, and the plasma current, and with the calculated value of $N_{||2}$ =

1.85 for the 90º spectrum we obtain for the parameter A values of between 0.84 and 1.02, or 0.46 and 0.59 for the lower and higher density points, respectively. Shown as dashed lines are the calculated curves, eq.(6), with A = 0.5; T = 1.1 and A = 1.0; T = 2.2. These values of T agree roughly with what we estimate from the increase in electron temperature at high RF power. However, at low density and low RF power (< 150 kW) the variation of the bulk temperature is not sufficient to explain the strong drop in loop voltage. In this situation the loop voltage is still high enough to make the fastest wave-generated electrons tend to run away. This can be clearly seen in the increase of the runaway signal at low RF power; in contrast, it rapidly decreases at high power and correspondingly low loop voltage.

The model was further checked by changing the other parameters contained in A, namely I_p and $N_{||2}$, and similar agreement was found /5/.The model was also found to be suitable for describing the loop voltage drop observed when a symmetric spectrum of waves is launched, or when the RF current is driven opposite to the inductively driven current.

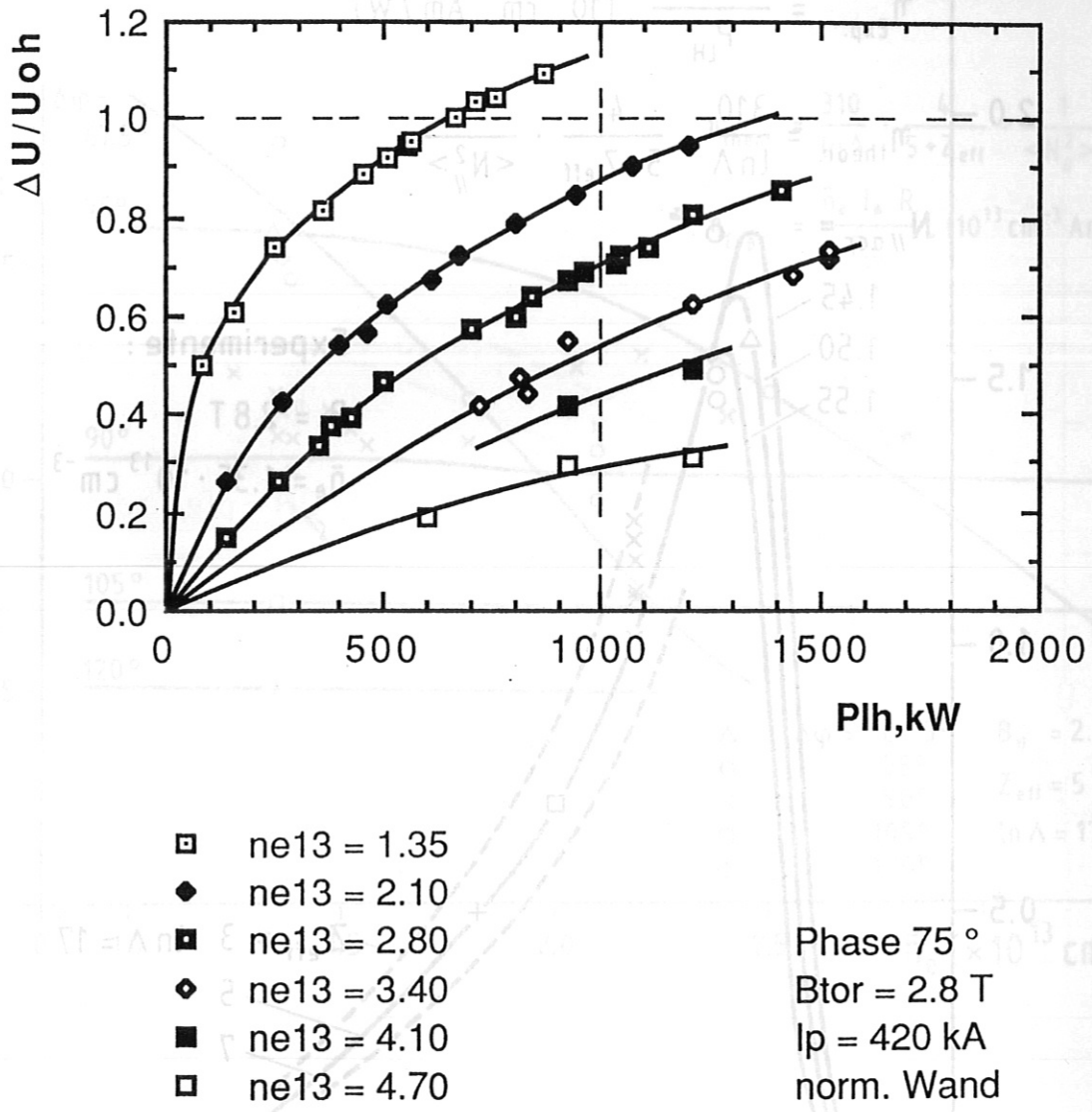

Fig. 5: Loop voltage drop $\Delta U/U_{OH}$ as a function of the power and different electron densities for LH current drive.

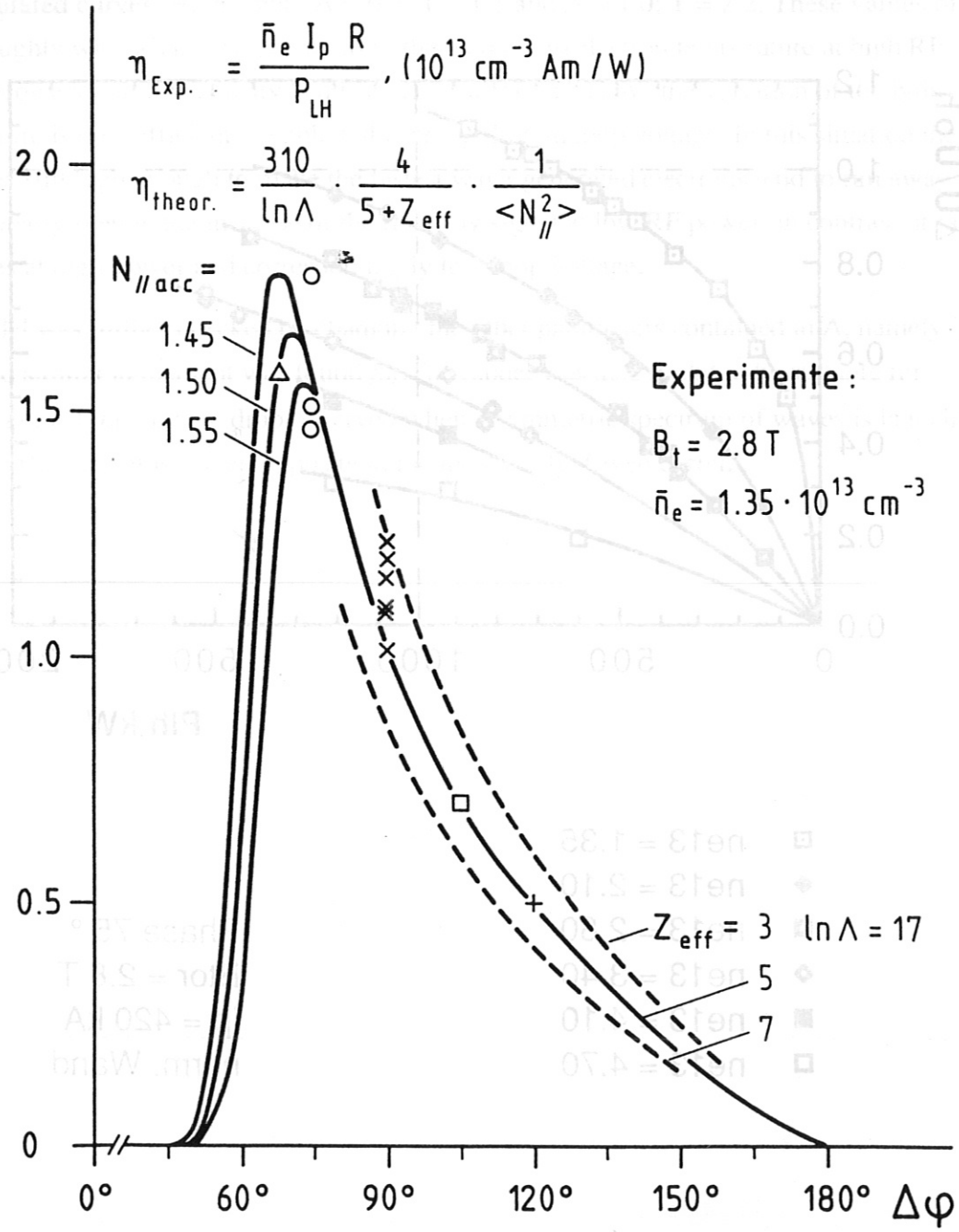

Fig. 6: Comparison of experimental current drive efficiencies with theory at low density, $\bar{n}_e = 1.35 \cdot 10^{13}\ cm^{-3}$.

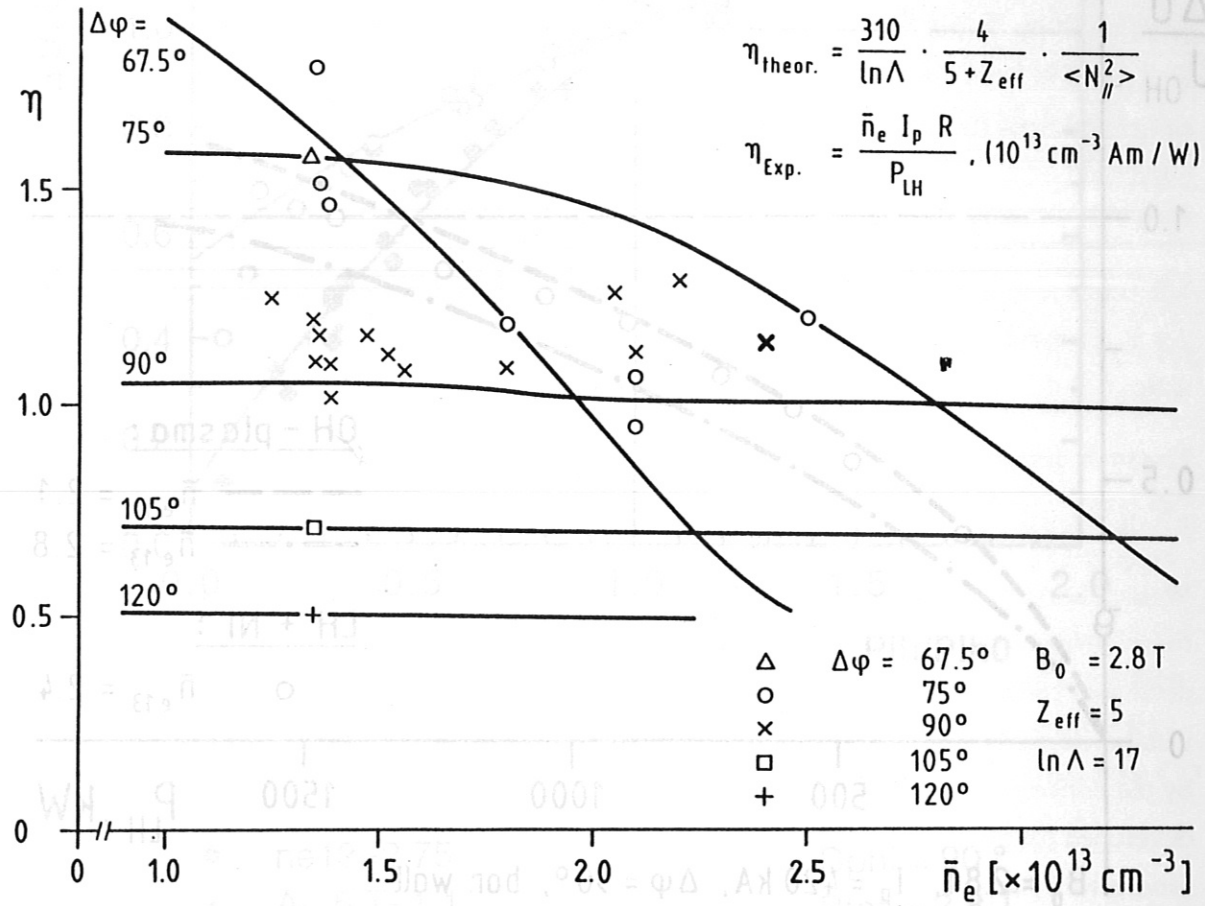

Fig. 7: Density dependence of experimental current drive efficiencies and comparison with theory.

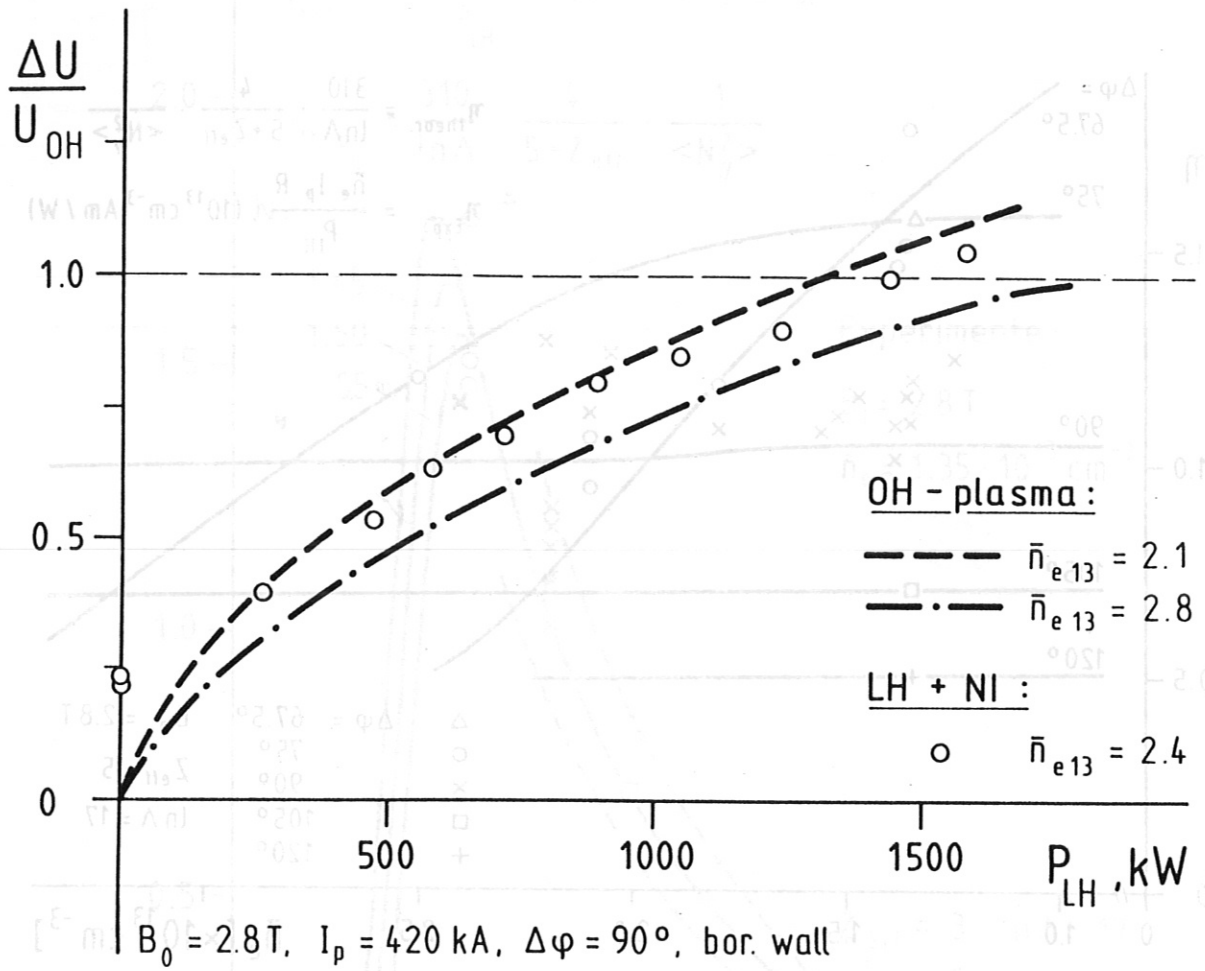

Fig. 8: Loop voltage drop $\Delta U/U_{OH}$ as a function of the power for LH current drive in a neutral-beam-heated plasma ($P_{NI} \approx 1$ MW) and comparison with current drive in an ohmically heated plasma (dashed lines).

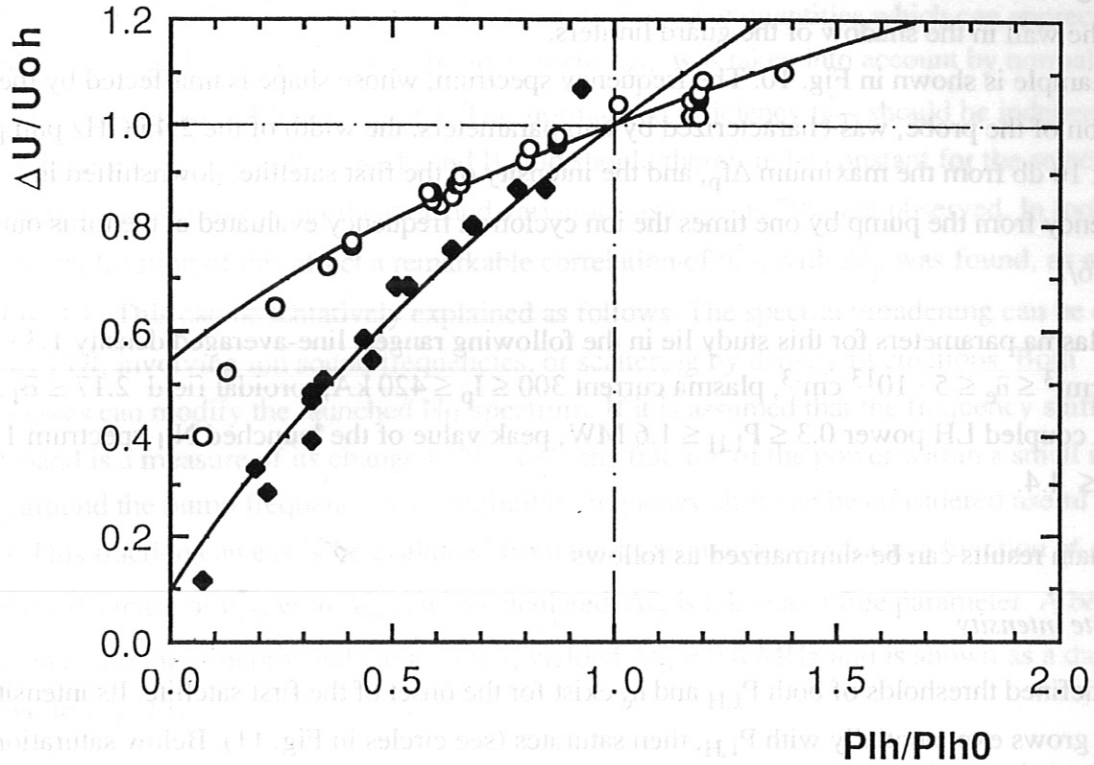

Fig. 9: Comparison of experimental loop voltage drop $\Delta U / U_{OH}$ with theory of electric field dependent current drive efficiency.

4. Parametric decay instabilities

A search for possible effects of parametric decay instabilities (PDI) on LH current drive and heating was conducted on ASDEX by analysis of the signal collected by an RF probe located near the wall in the shadow of the guard limiters.
An example is shown in Fig. 10. The frequency spectrum, whose shape is unaffected by the position of the probe, was characterized by two parameters: the width of the 2.45 GHz pump line at 10 db from the maximum Δf_p, and the intensity of the first satellite, downshifted in frequency from the pump by one times the ion cyclotron frequency evaluated at the torus outer edge /6/.

The plasma parameters for this study lie in the following ranges: line-averaged density $1.3 \cdot 10^{13}\ cm^{-3} \leq \bar{n}_e \leq 5 \cdot 10^{13}\ cm^{-3}$, plasma current $300 \leq I_p \leq 420$ kA, toroidal field $2.17 \leq B_t \leq 2.8$ T, coupled LH power $0.3 \leq P_{LH} \leq 1.6$ MW, peak value of the launched $N_{||}$ spectrum $1.5 \leq \bar{N}_{||} \leq 4.4$.

The main results can be summarized as follows

Satellite intensity

Well-defined thresholds of both P_{LH} and $\bar{n}_e$ exist for the onset of the first satellite. Its intensity firstly grows exponentially with P_{LH}, then saturates (see circles in Fig. 11). Below saturation it decreases considerably if either I_p or B_t are increased. The threshold for the growth of these instabilities is determined by the edge plasma density and temperature, the coupled power and by the convective losses, determined in turn by the grill dimensions. A code previously developed for the FT experiment, which takes into account all the above parameters, can satisfactorily reproduce the behaviour of the threshold power, as seen by the full circles in Fig. 12. With this same code the different developments of PDI, when either one or both rows of the grill are excited, are also well explained /7/.

The growth of one or more ion cyclotron satellites does not seem to affect greatly the current drive properties of the LH wave, at least not as long as they are 15 db below the pump, as is most often the case, except for higher density plasmas, $\bar{n}_e \geq 4.7 \cdot 10^{13}\ cm^{-3}$.

Pump spectral broadening

Triangles in Fig. 11 and Fig. 12 describe the behaviour of Δf_p versus P_{LH} and $\bar{n}_e$, respectively. An approximately linear increase is observed in either case. The influence of B_t and I_p is similar to the ion cyclotron PDI case, namely Δf_p decreases, increasing either B_t or I_p. The state of the walls is also important; indeed Δf_p became smaller after the ASDEX vacuum vessel was boronized.

Unlike the ion cyclotron sidebands, the magnitude of Δf_p appears to have a considerable effect on the current drive properties of the LH waves. This was established by analysis of CD efficiency values η_{CD} on a large data base selected in such a way as to avoid the problem of the LH wave accessibility to the plasma core. The effect of other quantities which can appreciably modify η_{CD}, such as $\bar{N}_{||}$ and the impurity content Z_{eff}, was taken into account by normalizing η_{CD} to the case $\bar{N}_{||} = 1.8$ and $Z_{eff} = 1$. This normalized efficiency η^*_{CD} should be independent of plasma parameters such as $\bar{n}_e$, I_p and B_t and should therefore be constant for the selected data set. However this is not the case and variations as large as 50% are observed. In looking for an explanation of this effect a remarkable correlation of η^*_{CD} with Δf_p was found, as shown in Fig. 13. This can be tentatively explained as follows. The spectral broadening can be due to either PDI, involving ion sound frequencies, or scattering by density fluctuations. Both processes can modify the launched $N_{||}$ spectrum. If it is assumed that the frequency shift of a sideband is a measure of its change in $N_{||}$, only the fraction of the power within a small interval Δf_0 around the pump frequency with negligible frequency shift can be considered useful for CD. This fraction can easily be evaluated from the experimental spectra as a function of Δf_p, and the decrease of η^*_{CD} with Δf_p can be calculated. Δf_0 is taken as a free parameter. A best-fit procedure on the experimental value of η^*_{CD} yielded $\Delta f_0 = 0.8$ MHz and is shown as a dashed curve in Fig. 13.

In conclusion, it has been shown that ion cyclotron PDIs are rather well understood since their behaviour can be satisfactorily predicted by the theory. They are found to have no great effect on the CD efficiency. On the contrary, pump spectral broadening considerably degrades the CD efficiency probably because of a related change in the launched $N_{||}$ spectrum.

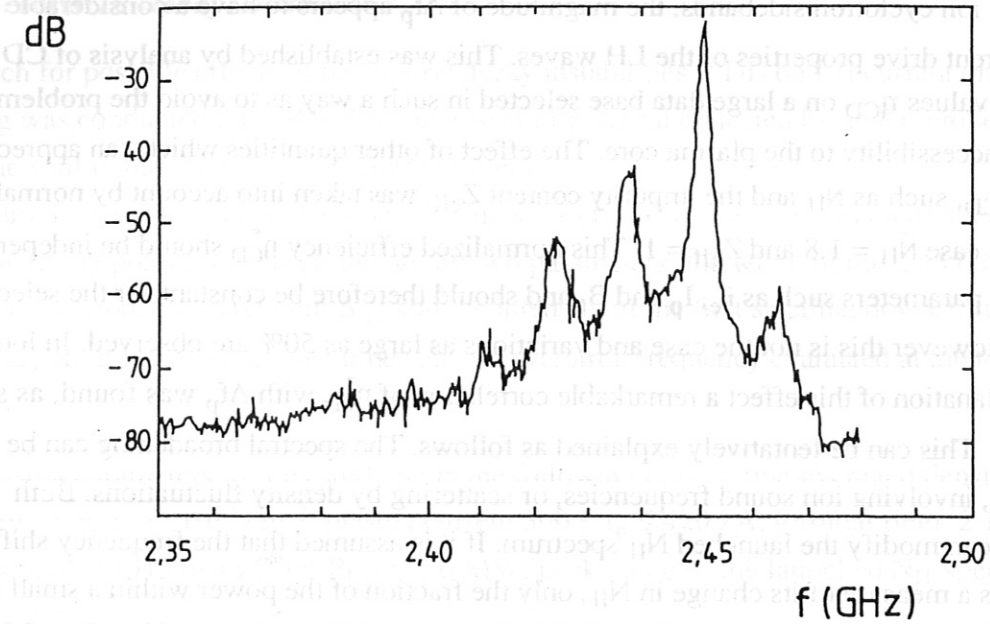

Fig.10: Typical parametric decay spectrum for well-developed instabilities.

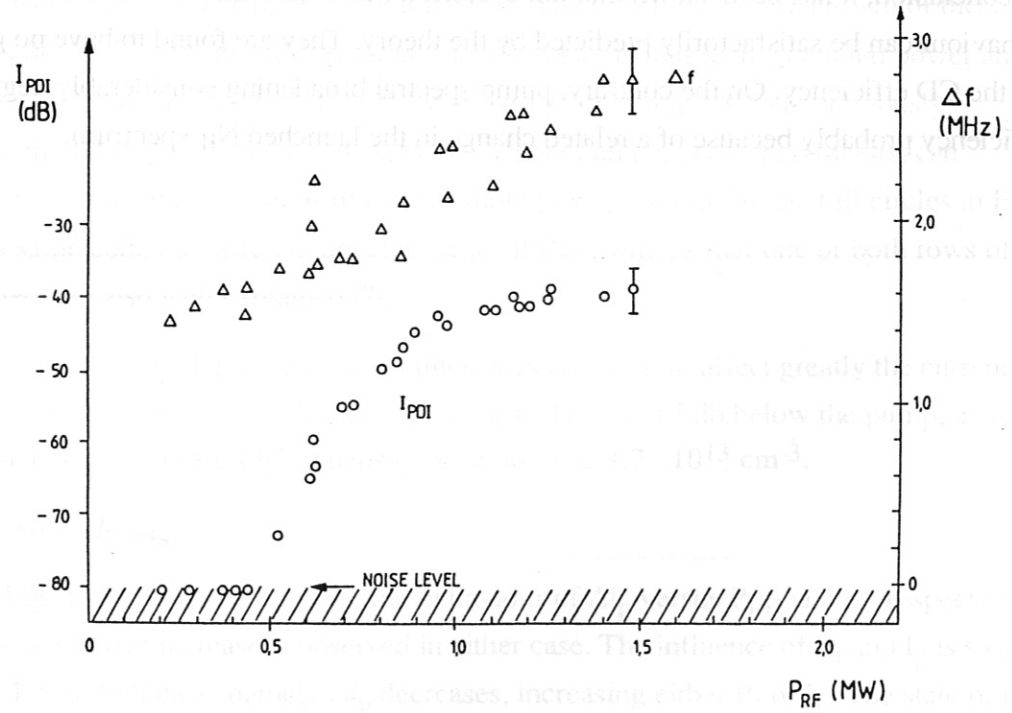

Fig.11: Plot of the pump spectral broadening (Δ) and of the first satellite intensity (O) versus the coupled LH power. $\bar{N}_{||} = 1.8$, $\bar{n}_e \leq 2.7 \cdot 10^{13}$ cm^{-3}, $I_p = 320$ kA, $B_t = 2.17$ T.

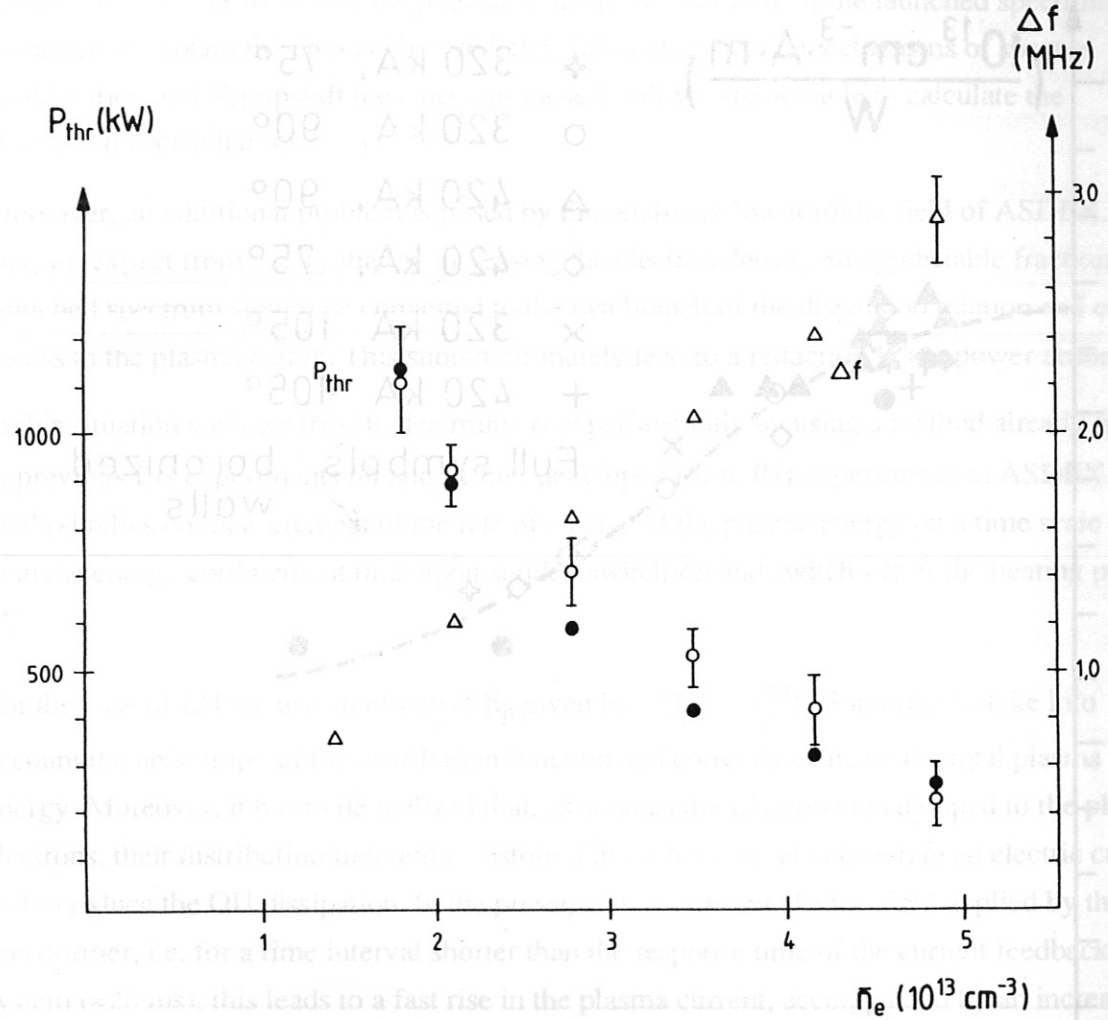

Fig.12: Experimental (O) and calculated (o) power thresholds versus $\bar{n}_e$, and pump spectral width (Δ) for P_{LH} = 1 MW, I_p = 420 kA, B_t = 2.8 T, $\bar{N}_{||}$ = 1.8.

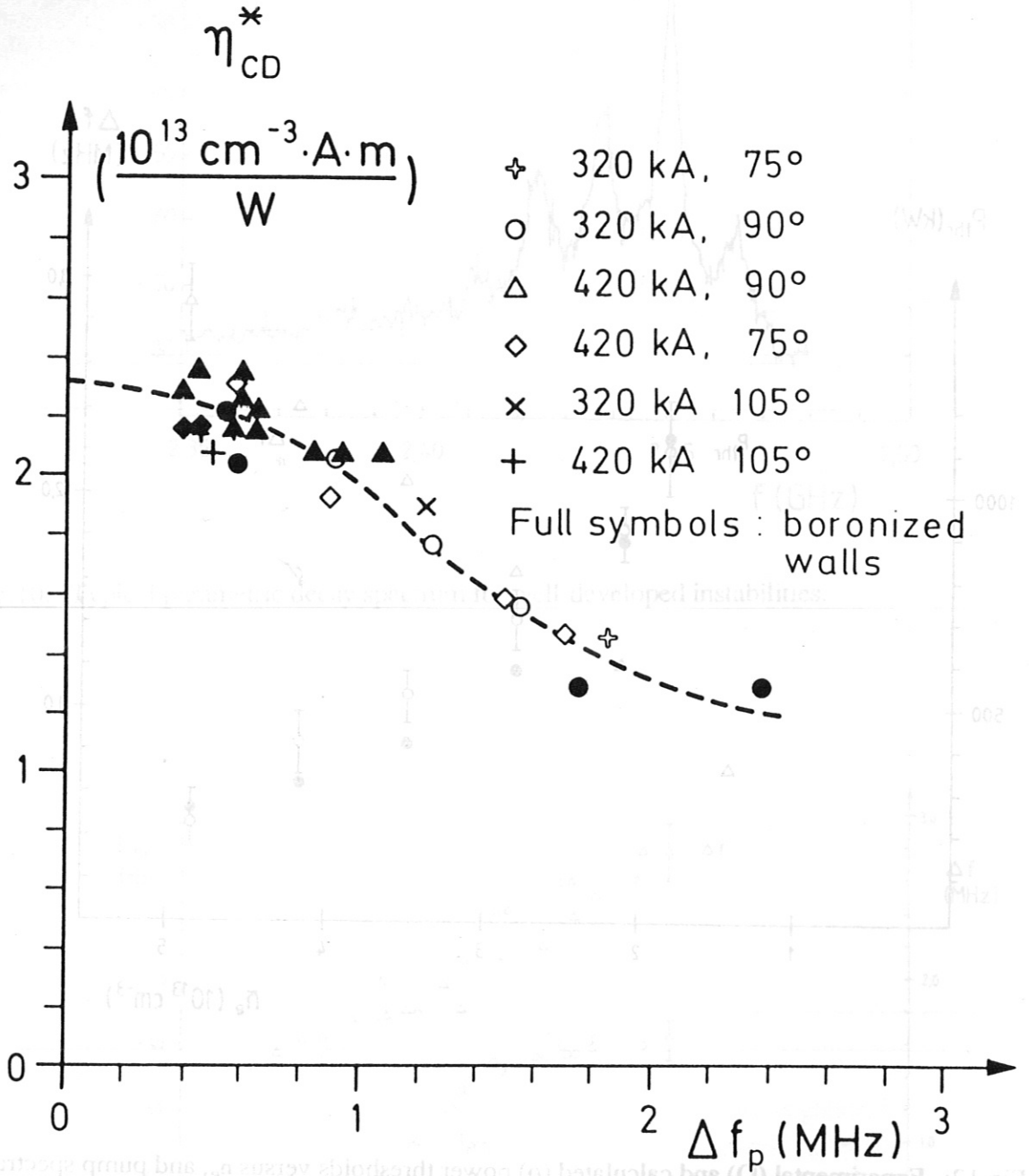

Fig.13: Normalized CD efficiency plotted versus the pump spectral width. The dashed curve is the fit with the simple model described in the text.

5. Power absorption

In the analysis of LH heating and current drive experiments, in contrast to the case of other heating methods and notably of neutral injection, we have no theory which can predict the amount of power absorbed by the plasma. Quasilinear damping of the launched spectrum is not sufficient to explain the effects observed and, although different mechanisms of spectral modification and $N_{||}$ upshift have been proposed, still we are not able to calculate the absorption coefficient α.

Moreover, an additional problem is posed by the relatively low toroidal field of ASDEX. In fact, we expect from theory that by increasing the electron density an appreciable fraction of the launched spectrum should be converted to the fast branch of the dispersion relation and cannot access to the plasma centre. This should ultimately lead to a reduction in the power absorption.

In this situation we have tried to determine α experimentally by using a method already applied in previous LH experiments /8/ and further developed for ICRH experiments in ASDEX. This method relies on measurement of the rate of change of the plasma energy on a time scale shorter than the energy confinement time upon sudden switch-on and switch-off of the heating pulse /9/.

For the case of LH we use an effective β_p given by $(2\beta_p^{equ} + \beta_p^{dia}) / 3$ in order to take into account the anisotropy of the distribution function and correctly evaluate the total plasma energy. Moreover, it has to be realized that, as soon as the LH power is damped to the plasma electrons, their distribution function is distorted in such a way as to generate an electric current and to reduce the OH dissipation. In the presence of a constant electric field applied by the OH transformer, i.e. for a time interval shorter than the response time of the current feedback system (≈20 ms), this leads to a fast rise in the plasma current, accompanied by an increase in the plasma magnetic energy, which has to be taken into account in the power balance.

We therefore evaluated our absorption coefficient from the rate of change in the total plasma energy, kinetic, as given by the effective β_p, and magnetic, as given by the total inductance of the plasma loop (internal and external). However, when considering the experimental results, we have to bear in mind that the power deposited far from the plasma centre will be dissipated on a time scale shorter than the time resolution of our diagnostics and is not detected. By using appropriate values for the relevant parameters, we estimate that our method is able to measure the power absorbed within $r \leq 30$ cm.

At low density ($\bar{n}_e \approx 1.3 \cdot 10^{13}$ cm^{-3}) we find that all power in the main peak of the spectrum is absorbed by the plasma core in current drive experiments. This is in agreement with the results on current drive efficiency, which are very close to their maximum theoretical value given by

total absorption. In this respect the power in the secondary lobe has too high a $N_{||}$ to contribute to the driven current and is very likely absorbed at the plasma edge. At this low density, α is higher for the lower $N_{||}$. By inverting the direction of the launched waves, i.e. by operating in opposite current drive conditions, we observe a reduction by a factor of about 2 in the power absorption. Intermediate results are obtained in experiments with symmetric spectra. These observations suggest that the applied d.c. electric field can play an important role in determining the wave absorption.

When we increase the plasma density, we find a remarkable decrease of α, in particular at lower magnetic field, as expected from accessibility considerations and as already found for the 1.3 GHz experiment /10/. In Fig. 14 we show the results of a density scan with $B_t = 2.17$ T and compare them with the fraction of power satisfying the accessibility condition at a plasma density equal to the line-averaged density and a magnetic field equal to the toroidal field on axis. From this it can be concluded that the decrease in α is related to degradation of the accessibility, although absorption is also found in cases where no power should reach the plasma core.

The measured absorption coefficient does not show any appreciable dependence on the launched power. Moreover, at intermediate density ($\bar{n}_e \approx 2.1 \cdot 10^{13}$ cm^{-3}) we changed $N_{||}$ and the width of the spectrum without appreciably changing the value of α. For $\bar{N}_{||} = 1.8$ and the same density we also changed the plasma current in order to vary the q-profile, which should influence the wave trajectory in the plasma. But this did not affect α either.

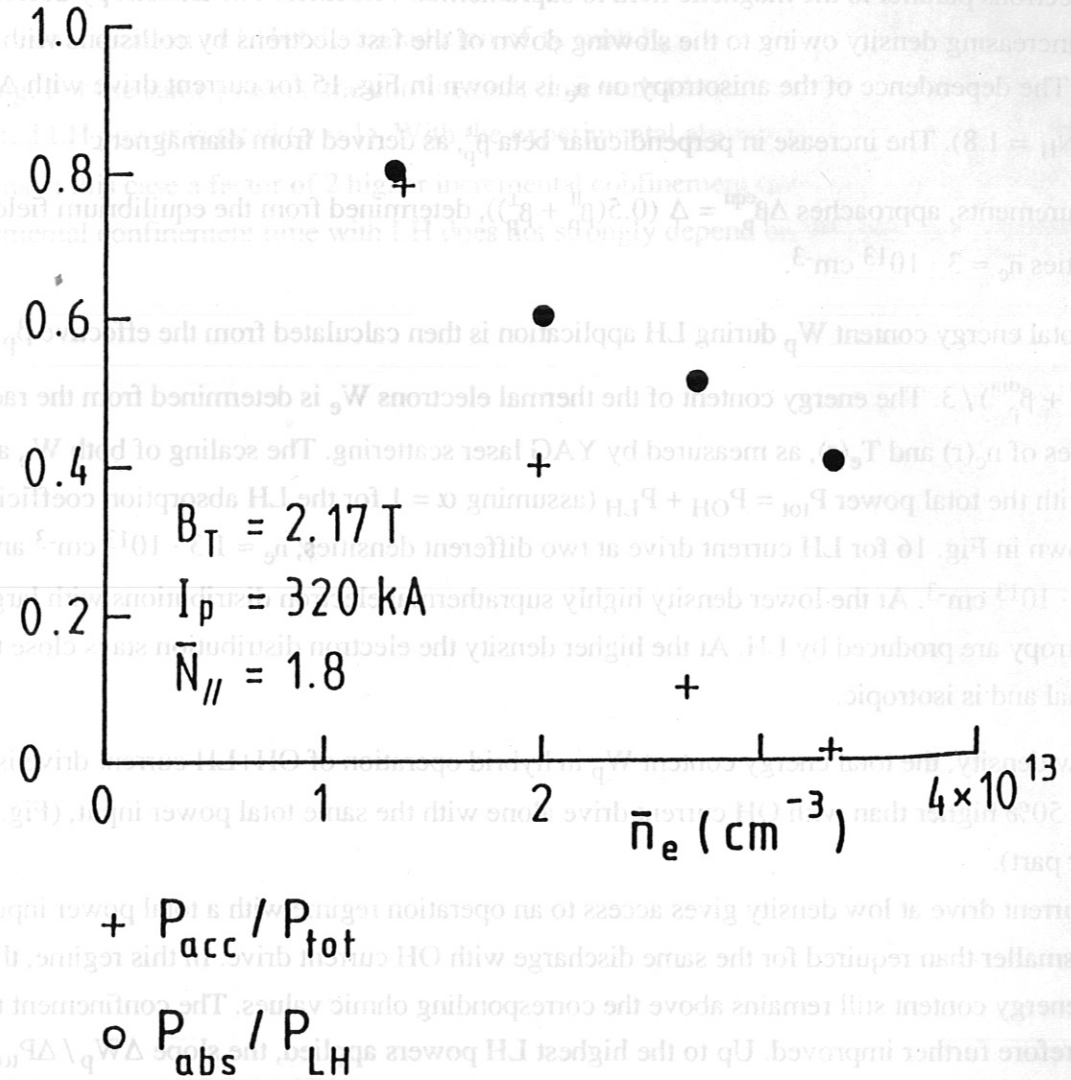

Fig. 14: Density dependence of the absorption coefficient for LH power and of the accessible fraction of LH power.

6. *Energy confinement*

Anisotropic electron distributions are generated with LH spectra of low $N_{||}$, which accelerate the electrons parallel to the magnetic field to suprathermal velocities. The anisotropy decreases with increasing density owing to the slowing down of the fast electrons by collisions with the bulk. The dependence of the anisotropy on $\bar{n}_e$ is shown in Fig. 15 for current drive with $\Delta\varphi = 75^o$ ($\bar{N}_{||} = 1.8$). The increase in perpendicular beta $\beta_p^{\perp}$, as derived from diamagnetic measurements, approaches $\Delta\beta_p^{equ} = \Delta\,(0.5(\beta_p^{||} + \beta_p^{\perp}))$, determined from the equilibrium fields, at densities $\bar{n}_e \approx 3 \cdot 10^{13}$ cm^{-3}.

The total energy content W_p during LH application is then calculated from the effective $\beta_p = (2\beta_p^{equ} + \beta_p^{dia}) / 3$. The energy content of the thermal electrons W_e is determined from the radial profiles of $n_e(r)$ and $T_e(r)$, as measured by YAG laser scattering. The scaling of both W_p and W_e with the total power $P_{tot} = P_{OH} + P_{LH}$ (assuming $\alpha = 1$ for the LH absorption coefficient) is shown in Fig. 16 for LH current drive at two different densities, $\bar{n}_e \approx 1.3 \cdot 10^{13}$ cm^{-3} and $\bar{n}_e \approx 3.5 \cdot 10^{13}$ cm^{-3}. At the lower density highly suprathermal electron distributions with large anisotropy are produced by LH. At the higher density the electron distribution stays close to thermal and is isotropic.

At low density, the total energy content W_p in hybrid operation of OH+LH current drive is about 50% higher than with OH current drive alone with the same total power input, (Fig. 16, upper part).

LH current drive at low density gives access to an operation regime with a total power input even smaller than required for the same discharge with OH current drive. In this regime, the total energy content still remains above the corresponding ohmic values. The confinement time is therefore further improved. Up to the highest LH powers applied, the slope $\Delta W_p / \Delta P_{tot}$ stays the same. Over the whole range of powers, also in the regime $P_{tot} < P_{OH}$, the same incremental energy confinement time τ_E^{inc} is then obtained. Its value is smaller than the ohmic confinement time. The global confinement time therefore degrades continuously with power, starting already at $P_{tot} < P_{OH}$. The dependence of τ_E on P_{tot} is well fitted by Goldston scaling and Lackner plateau scaling. For the thermal energy content of the electrons W_e no increase above the ohmic value is found with hybrid operation of LH+OH current drive with the same total power input as in ohmic discharges. The thermal ion energy content, as determined by CX analysis, also remains the same in both cases. The improvement in global confinement, seen from the enhanced W_p , can therefore only be attributed to superior energy confinement of the suprathermal electron population. In fact, with increasing density and thereby a decreasing fraction of LH-produced fast electrons the improvement of global energy confinement with LH

disappears /11/. At a density of $\bar{n}_e \approx 3.5 \cdot 10^{13}$ cm^{-3} no enhancement of W_p above OH values is obtained. The total power input also always exceeds the input power of the OH phase (Fig. 16, lower part). At this density the electron distribution is isotropic (Fig. 15).

With a combination of LH+NI, degradation of τ_E with P_{tot} is found consistently with Goldston scaling. For the same powers, the confinement time with LH is comparable with NI if the total injected LH power is rated ($\alpha = 1$). With the experimental absorption coefficient $\alpha \approx 0.5$ one obtains in this case a factor of 2 higher incremental confinement times than with NI. The incremental confinement time with LH does not strongly depend on the plasma current.

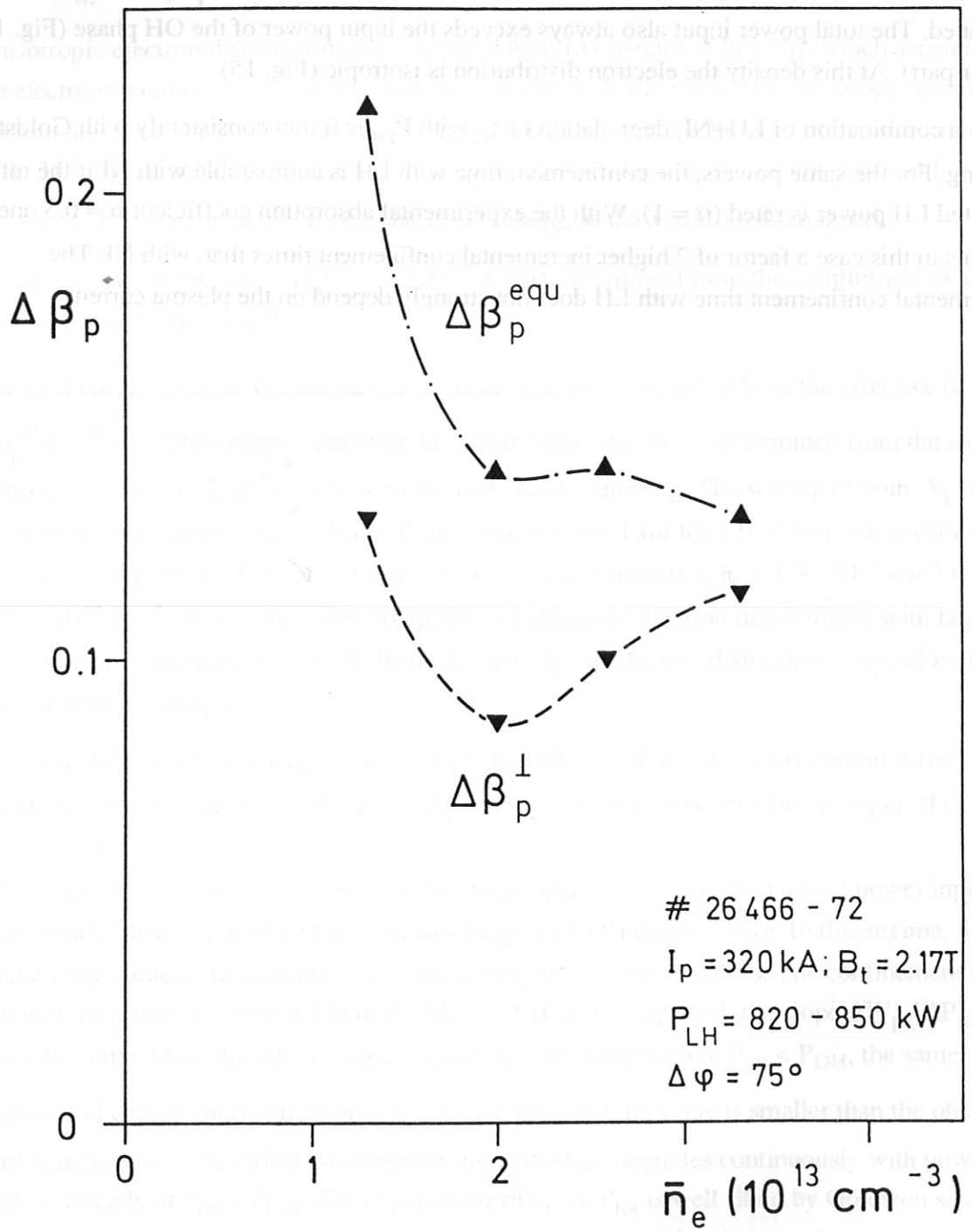

Fig. 15: Variation of the increments of diamagnetic beta ($\Delta\beta_p^{\perp}$) and equilibrium beta ($\Delta\beta_p^{equ}$) with density for LH current drive.

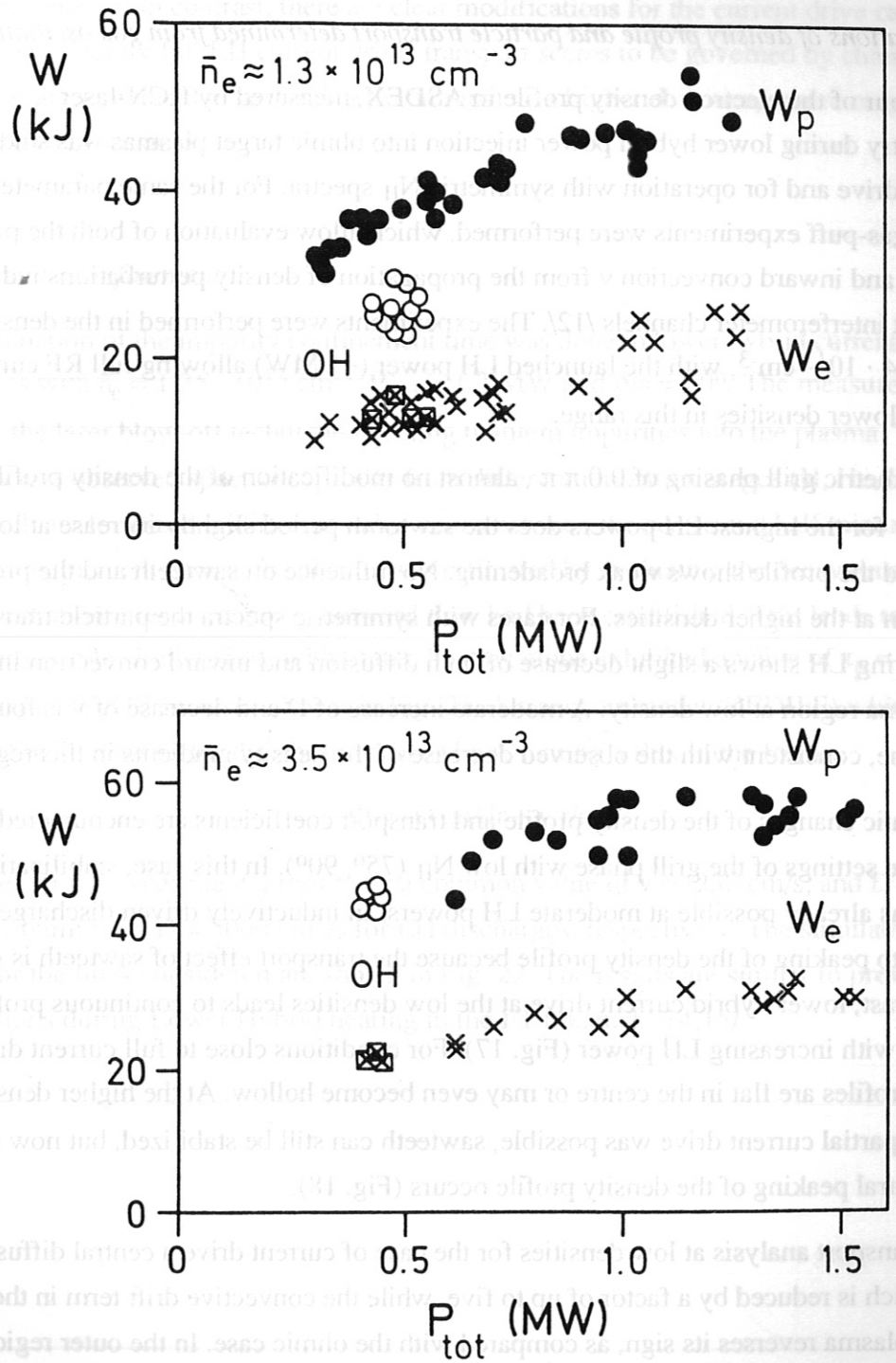

Fig. 16: Total energy content W_p and thermal electron energy content W_e versus total power $P_{tot} = P_{OH} + P_{LH}$ for LH current drive ($\Delta\varphi = 90^o$) at two different densities. $B_t = 2.8$ T, $I_p = 420$ kA.

7. *Particle confinement*

7.1 Modifications of density profile and particle transport determined from gas oscillations

The behaviour of the electron density profile in ASDEX, measured by HCN-laser interferometry during lower hybrid power injection into ohmic target plasmas was studied for LH current drive and for operation with symmetric $N_{||}$ spectra. For the same parameters oscillating gas-puff experiments were performed, which allow evaluation of both the particle diffusion D and inward convection v from the propagation of density perturbations induced in the different interferometer channels /12/. The experiments were performed in the density range $\bar{n}_e = 1.2 - 2.4 \cdot 10^{13}$ cm^{-3}, with the launched LH power (~1 MW) allowing full RF current drive at the lower densities in this range.

With a symmetric grill phasing of $0\ 0\ \pi\ \pi$, almost no modification of the density profile is found. Only for the highest LH powers does the sawtooth period slightly increase at low densities and the profile shows weak broadening. No influence on sawteeth and the profile shape is seen at the higher densities. For cases with symmetric spectra the particle transport analysis during LH shows a slight decrease of both diffusion and inward convection in the central plasma region at low density. A moderate increase of D and decrease of v is found in the gradient zone, consistent with the observed decrease of the density gradients in this region /13/.

More dramatic changes of the density profile and transport coefficients are encountered for current drive settings of the grill phase with low $N_{||}$ (75°, 90°). In this case, stabilization of sawteeth was already possible at moderate LH powers. In inductively driven discharges this would lead to peaking of the density profile because the transport effect of sawteeth is switched off. In contrast, lower hybrid current drive at the low densities leads to continuous profile broadening with increasing LH power (Fig. 17). For conditions close to full current drive (i.e. $E \approx 0$) the profiles are flat in the centre or may even become hollow. At the higher densities, where only partial current drive was possible, sawteeth can still be stabilized, but now the familiar central peaking of the density profile occurs (Fig. 18).

From the transport analysis at low densities for the case of current drive a central diffusion is inferred which is reduced by a factor of up to five, while the convective drift term in the inner part of the plasma reverses its sign, as compared with the ohmic case. In the outer region both D and v are slightly reduced, the convective term keeping its inward direction (Figs. 19 and 20). For partial current drive at densities above $2 \cdot 10^{13}$ cm^{-3} the central D is only moderately reduced and v stays nearly unchanged, while both parameters show an increase at larger radii. These transport modifications could explain the above-mentioned profile changes for current drive at different densities.

In conclusion, the analysis indicates only a small effect of LH power on particle transport for symmetric spectra. In contrast, there are clear modifications for the current drive case. At low densities with nearly full LH current drive, transport seems to be governed by changes initiated by current drive, while the sawtooth term dominates at higher densities, where only partial current drive is possible.

7.2. Impurity confinement

An examination of the impurity confinement time was done in lower hybrid current driven discharges with $\bar{n}_e = 1.35 \cdot 10^{13}$ cm^{-3}, $P_{LH} = 1.3$ MW and $\Delta\varphi = 90^o$. The measurements were made by the laser blow-off technique injecting titanium impurities into the plasma. Ti line radiation was observed spectroscopically from different ionization stages (H, He, Li and Be-like) which are localized in different radial zones between the centre and half minor radius. The titanium confinement time in the plasma was estimated by evaluating the decay times of its emitted radiation after a stationary outward flow had been established. This leads to a value of $\tau_p = 95$ ms, while similar shots with ohmic heating alone exhibited a value of $\tau_p = 49$ ms. Signals from Ti XXI lines are shown in Fig. 21. A transport model (ZEDIFF) which calculates the line intensities for the observed lines by assuming a flux in the form

$$\Phi = -D\, dn/dr + v\, r/a$$

can represent the experimental results by a common value of v = -230 cm/s, and D = 7500 cm^2/s for ohmic and D = 5000 cm^2/s for LH discharges, respectively. The simulated brightnesses for the lines considered are shown in Fig. 22. The results are similar to previous observations during Lower Hybrid heating in the FT tokamak /14,15/.

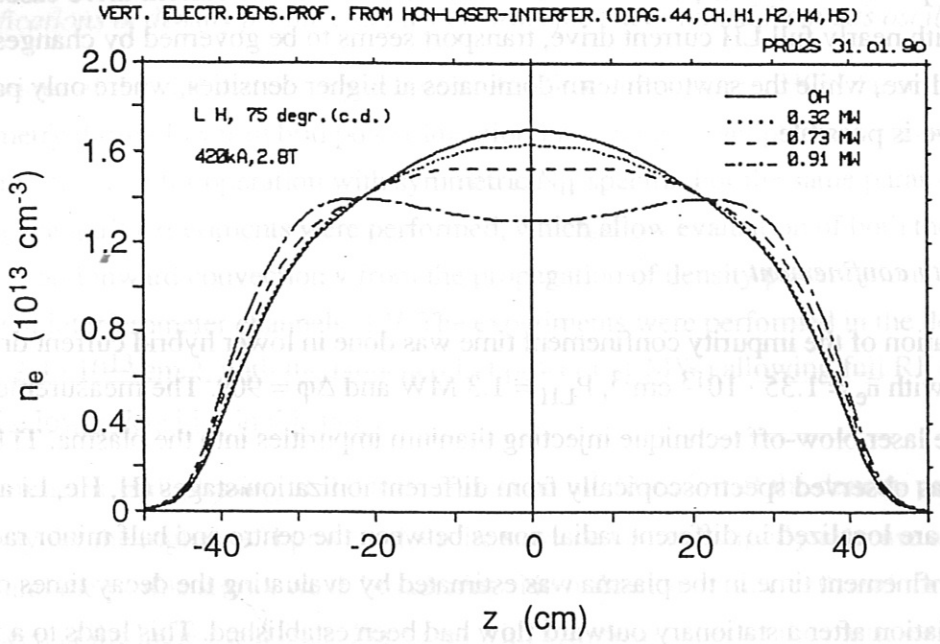

Fig. 17: Development of the electron density profile with increasing lower hybrid power, shown for current drive at an average density of $\bar{n}_e = 1.2 \cdot 10^{13}$ cm^{-3}.

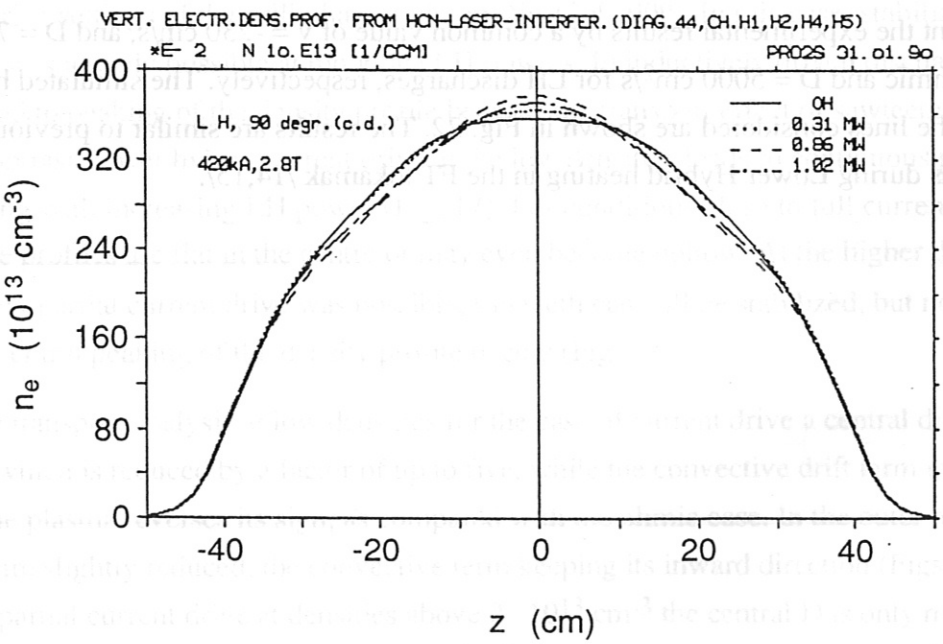

Fig. 18: Like Fig. 13, but shown for an average density of $\bar{n}_e = 2.2 \cdot 10^{13}$ cm^{-3}.

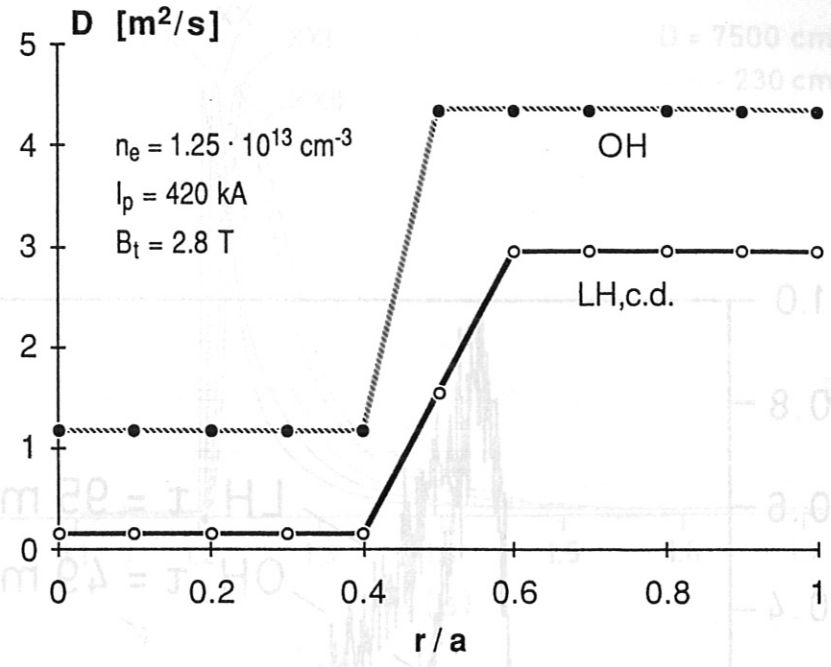

Fig. 19 Modifications of the radial behaviour of particle diffusion D for lower hybrid current drive, as compared to the ohmic case.

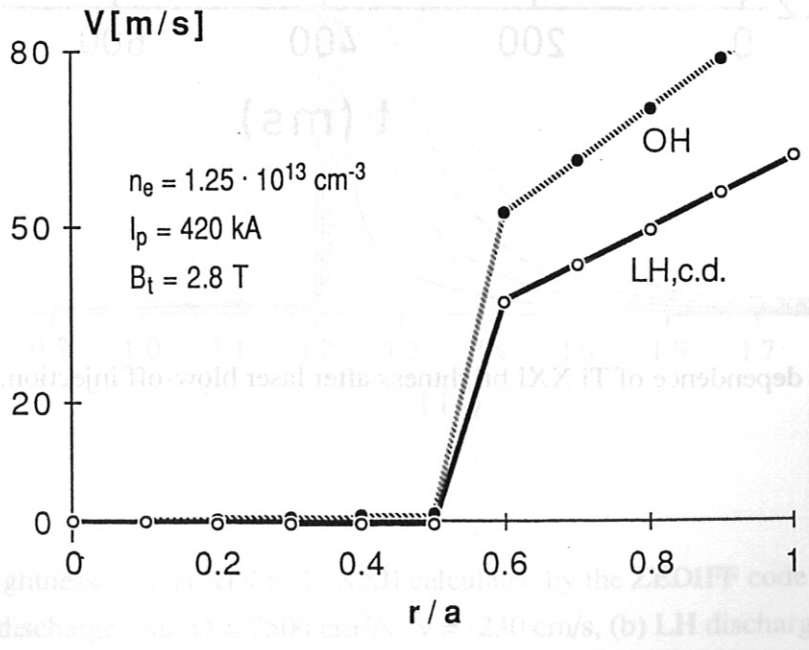

Fig. 20: Modifications of the radial behaviour of inward convection v for lower hybrid current drive, as compared to the ohmic case.

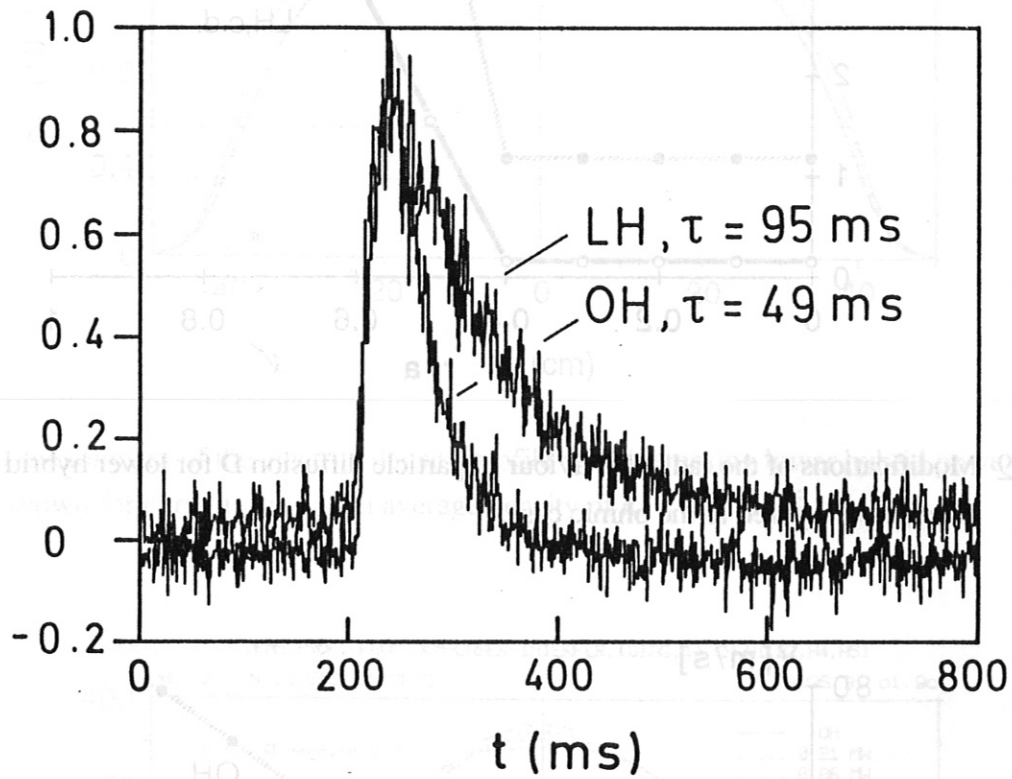

Fig. 21: Time dependence of Ti XXI brightness after laser blow-off injection.

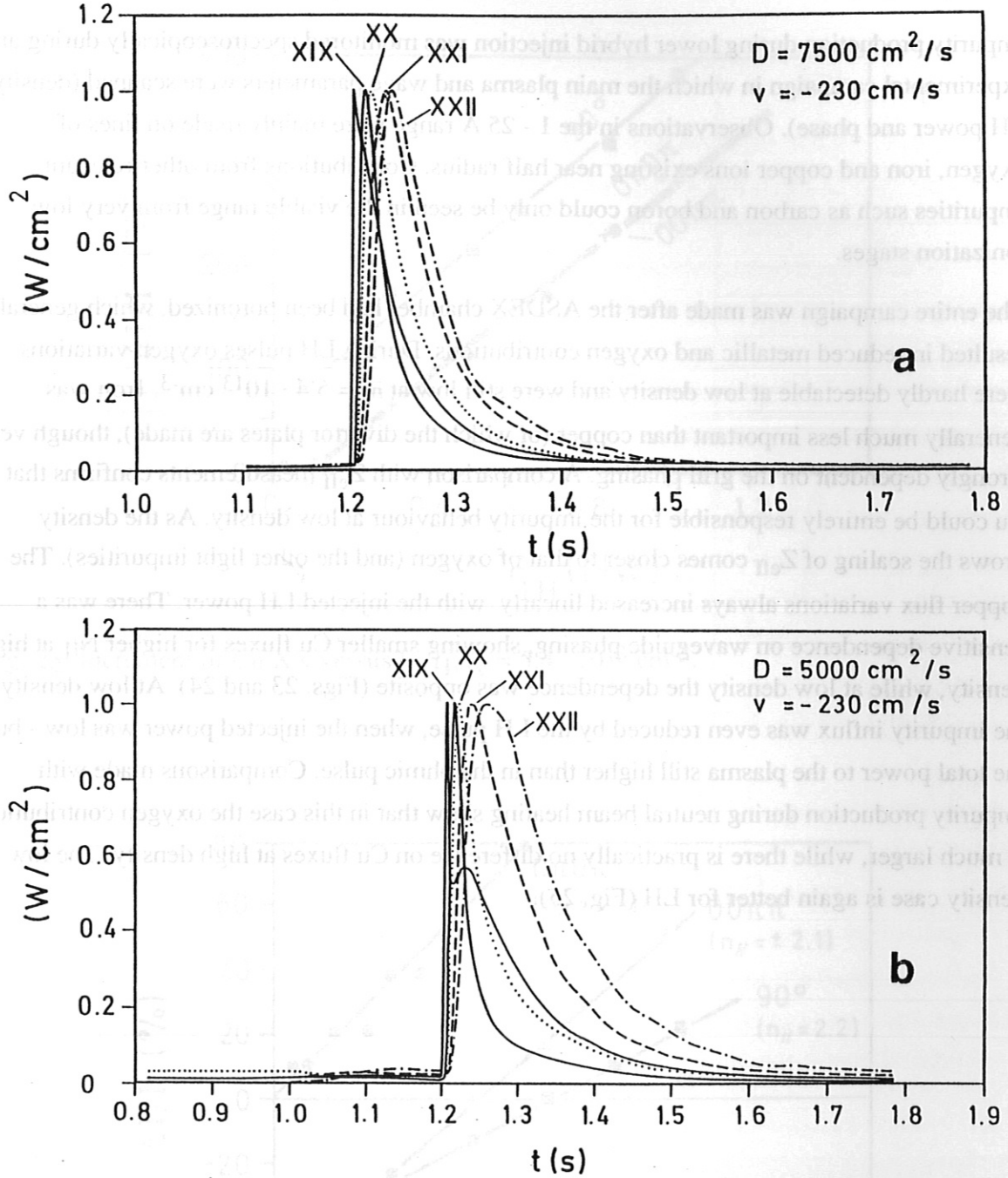

Fig. 22: Line brightnesses of Ti XIX to Ti XXII calculated by the ZEDIFF code to simulate (a) ohmic discharge with D = 7500 cm^2/s , v = -230 cm/s, (b) LH discharge with D = 5000 cm^2/s , v = -230 cm/s.

8. Impurity production

Impurity production during lower hybrid injection was monitored spectroscopically during an experimental campaign in which the main plasma and wave parameters were scanned (density, LH power and phase). Observations in the 1 - 25 Å range were mainly made on lines of oxygen, iron and copper ions existing near half radius. Contributions from other relevant impurities such as carbon and boron could only be seen in the visible range from very low ionization stages.

The entire campaign was made after the ASDEX chamber had been boronized, which generally resulted in reduced metallic and oxygen contributions. During LH pulses oxygen variations were hardly detectable at low density and were still low at $\bar{n}_e = 5.4 \cdot 10^{13}$ cm^{-3}. Iron was generally much less important than copper (of which the divertor plates are made), though very strongly dependent on the grill phasing. A comparison with Z_{eff} measurements confirms that Cu could be entirely responsible for the impurity behaviour at low density. As the density grows the scaling of Z_{eff} comes closer to that of oxygen (and the other light impurities). The copper flux variations always increased linearly with the injected LH power. There was a sensitive dependence on waveguide phasing, showing smaller Cu fluxes for higher $N_{||}$ at high density, while at low density the dependence was opposite (Figs. 23 and 24). At low density the impurity influx was even reduced by the LH pulse, when the injected power was low - but the total power to the plasma still higher than in the ohmic pulse. Comparisons made with impurity production during neutral beam heating show that in this case the oxygen contribution is much larger, while there is practically no difference on Cu fluxes at high density. The low density case is again better for LH (Fig. 25).

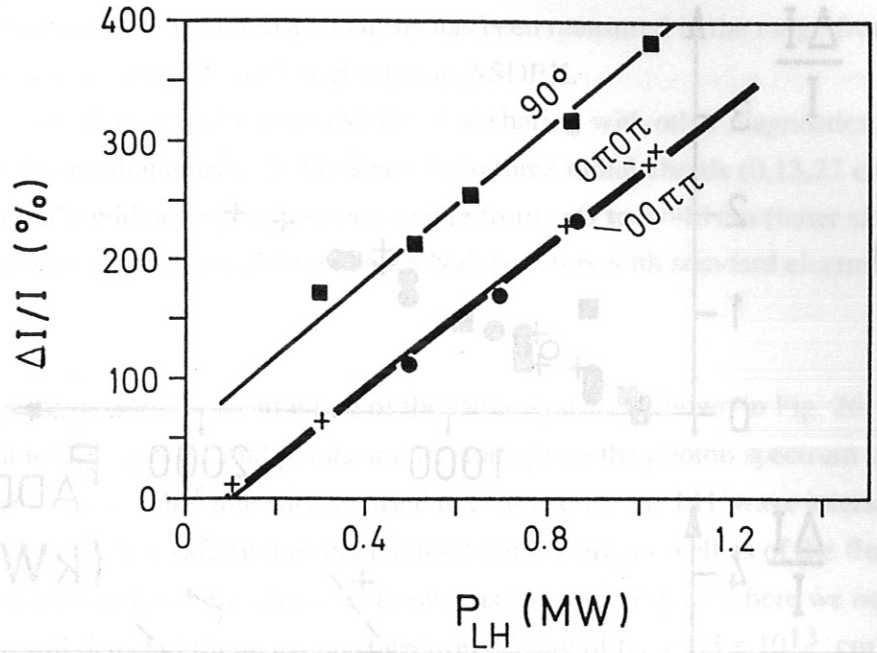

Fig. 23: Increment of Cu XX versus P_{LH}, $\bar{n}_e = 5.4 \cdot 10^{13}$ cm^{-3}.

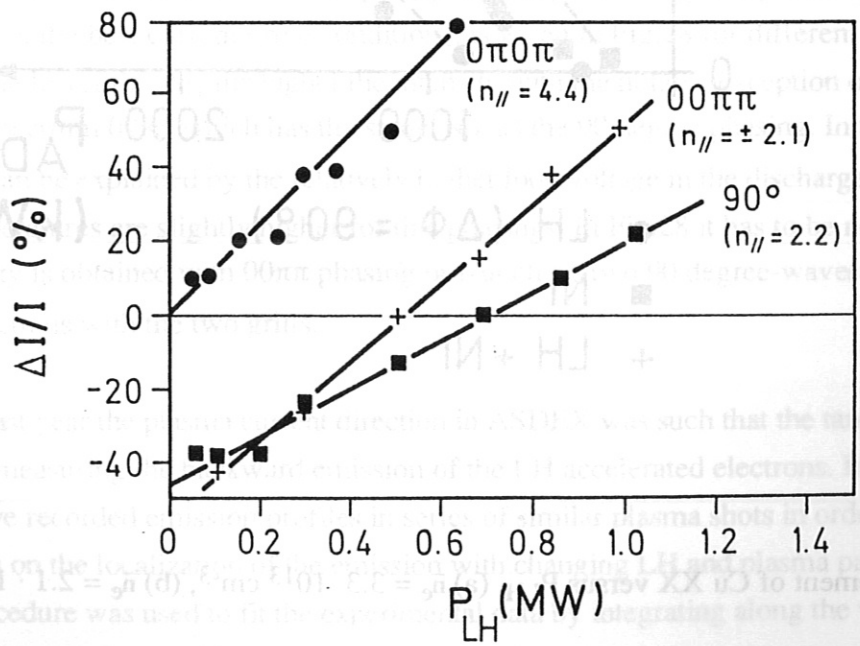

Fig. 24: Increment of Cu XX versus P_{LH}, $\bar{n}_e = 1.35 \cdot 10^{13}$ cm^{-3}.

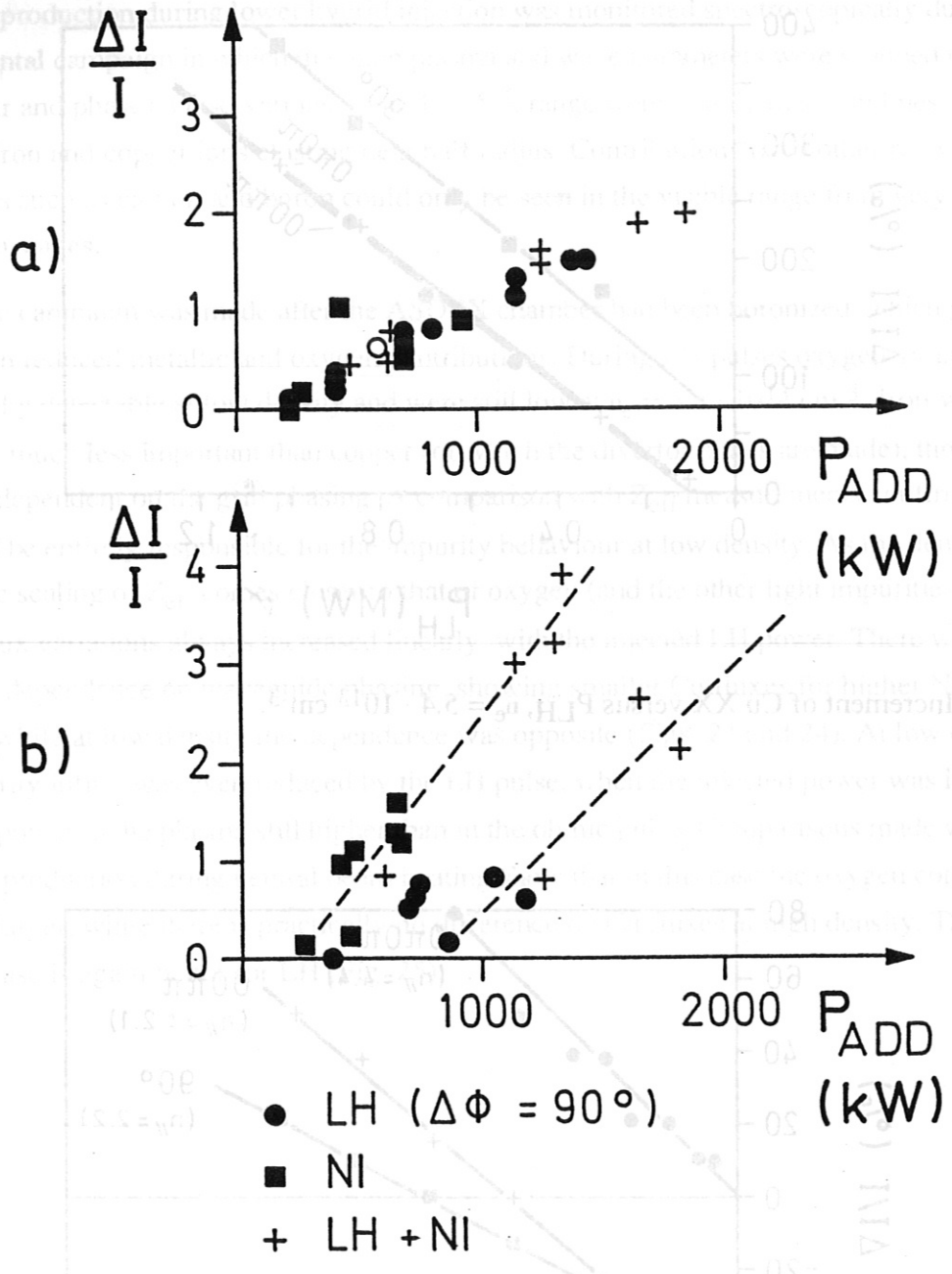

Fig. 25: Increment of Cu XX versus P_{LH}, (a) $\bar{n}_e = 3.3 \cdot 10^{13}$ cm^{-3}, (b) $\bar{n}_e = 2.1 \cdot 10^{13}$ cm^{-3}.

9. Hard X-ray emission

Bremsstrahlung emission from fast electrons has been measured in the range from 50 to 500 keV for a large fraction of the LH discharges in ASDEX.
During 1989 two systems have been used in time sharing with other diagnostics. The first system records simultaneously the emission from three radial chords (0,13,27 cm), the second looks tangentially with a tangency point variable from r=O to r=-40 cm (inner side) on a shot by shot basis. The two systems use three inches NaI detectors with standard electronics and data acquisition.

A typical spectrum from the central line of the radial system is shown in Fig. 26; the straight line is the best fit to the experimental points and its slope gives the photon spectrum temperature. This parameter and the flux intensity are used to characterize the LH wave interaction with electrons. The strongest variation of the photon temperature, as well as of the flux intensity, is found to be correlated with the electron density, as shown in Fig.27 where we note that fast electrons are still detected for an average electron density of $\bar{n}_e = 4.5 \times 10^{13}$ cm^{-3}. A smaller decrease is found with increasing $\bar{N}_{||}$ in the cases of current drive spectra and generally a radial decrease occurs only for the most peripherical chord. No major variations of the photon temperature are detected in the range of power that has been investigated or by changing the working gas.
A summary of the dependence of the hard-x ray intensity versus the LH power in low density discharges, i.e. the best current drive conditions, is given in Fig.28 for different phasings. It shows that the lower the $\bar{N}_{||}$ the higher the intensity with the notable exception of the symmetric spectrum $00\pi\pi$ which has the same $\bar{N}_{||}$ as the 90 degree phasing. In this case the higher flux can be explained by the relatively higher loop voltage in the discharge; also the photon temperatures are slightly higher for this phasings. In Fig.28 it has to be noted that the same intensity is obtained with $00\pi\pi$ phasing or launching two 90 degree-waves in opposite toroidal directions with the two grills.

During the last year the plasma current direction in ASDEX was such that the tangential system was always measuring the backward emission of the LH accelerated electrons. In these conditions we recorded emission profiles in series of similar plasma shots in order to obtain informations on the localization of the emission with changing LH and plasma parameters. An iterative procedure was used to fit the experimental data by integrating along the viewing chord a parametrized emission profile.
Two examples of this work are shown in the Fig.29 where the experimental intensity at 100 kev (open box) is plotted versus the tangency major radius. The full line is the computed

integral that fits best the experimental points and the dotted one is the calculated radial emission profile. The two cases shown refer to the same plasma conditions with two different LH current drive spectra, Fig.29a is a combined spectrum of low and high-$\bar{N}_{||}$ spectra ($\bar{N}_{||}$=2.2, 3.6), Fig.29b is a case with only the low-$\bar{N}_{||}$ spectrum ($\bar{N}_{||}$=2.2). From the two figures we deduce that for the spectra with higher $\bar{N}_{||}$ the experimental points are better fitted with a broader hard X-ray emission profile which is peaked off-axis. This suggests a broader radial distribution of the fast electrons generated by the injected LH waves. A similar dependence on the $N_{||}$ spectrum had been obtained at lower density in the experiments at 1.3 GHz /16/.

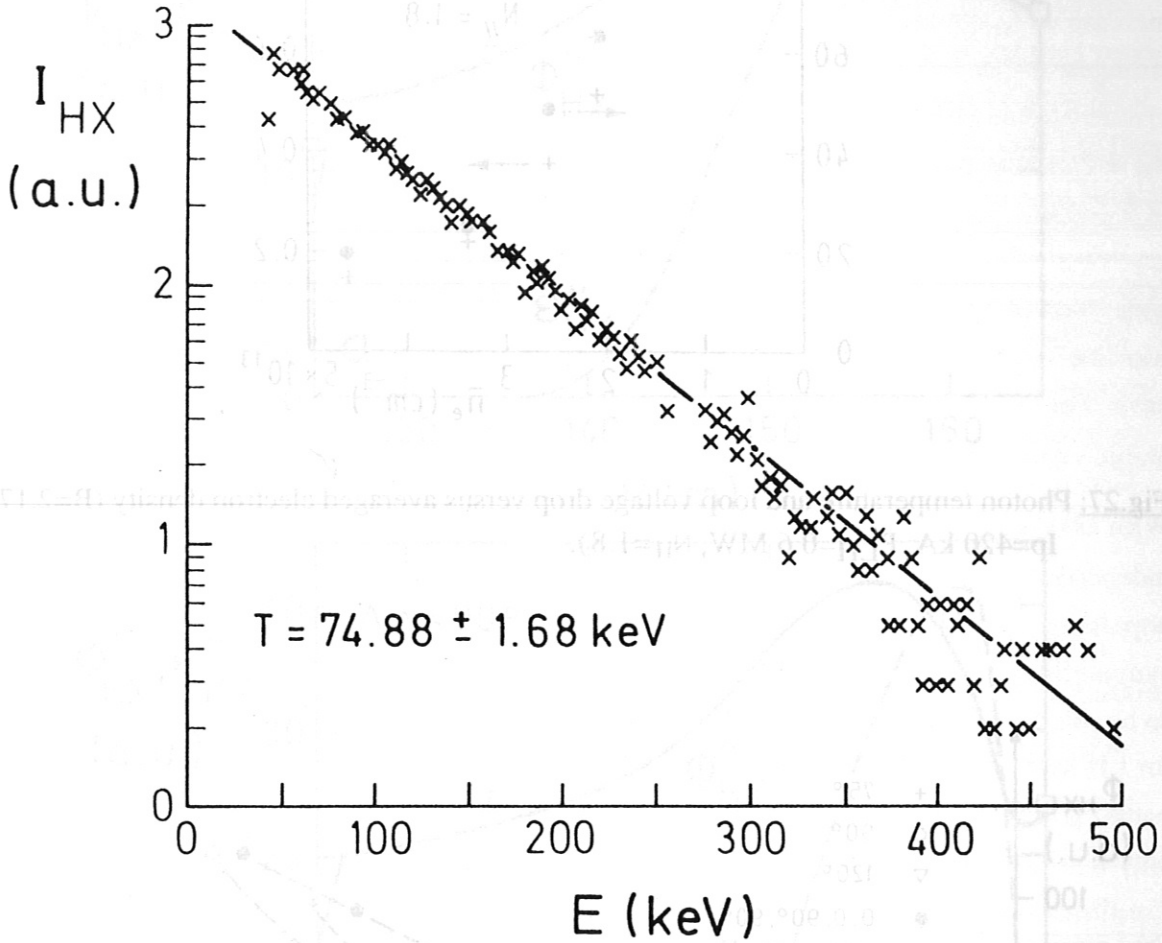

Fig.26: Typical hard-x ray spectrum from a central radial chord (B=2.8 T,Ip=420 kA,$\bar{n}_e$ = 1.5 x 10^{13} cm^{-3}, P_{LH}=0.6 MW, $\bar{N}_{||}$=1.8).

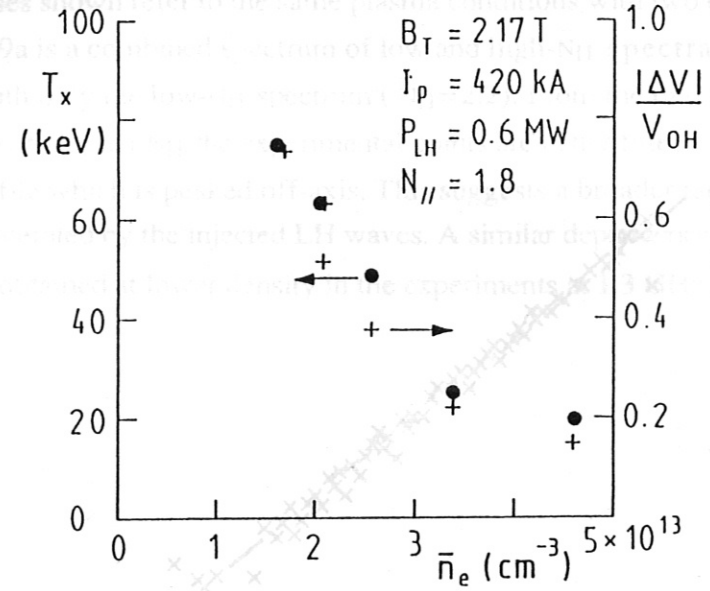

Fig.27: Photon temperature and loop voltage drop versus averaged electron density (B=2.17 T, Ip=420 kA, P_{LH}=0.6 MW, $\bar{N}_{//}$=1.8).

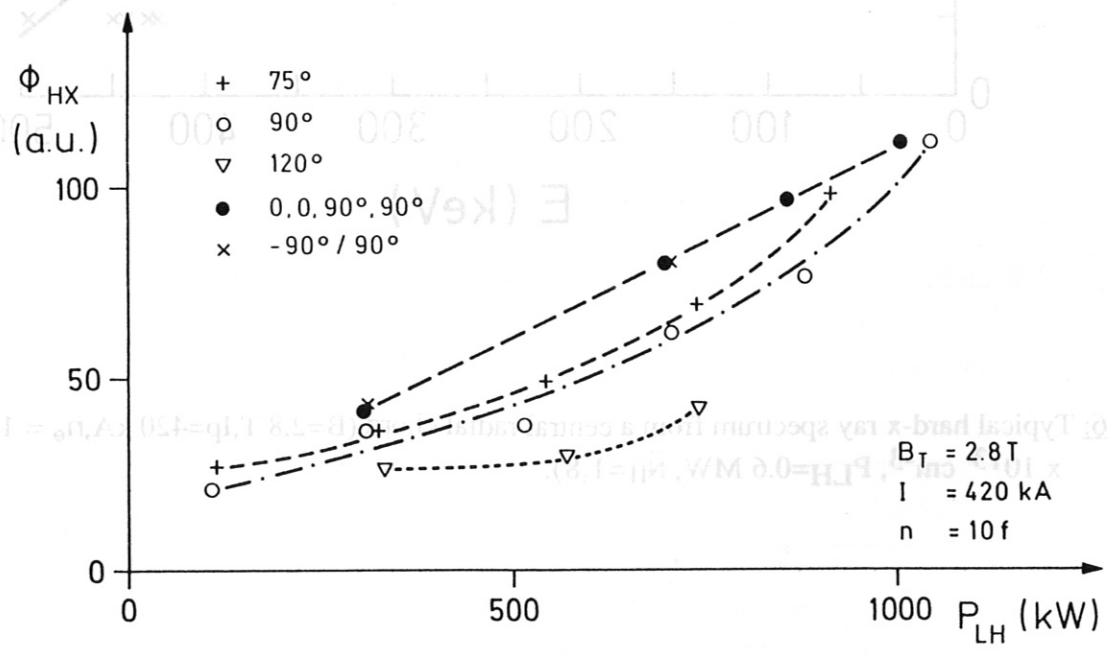

Fig.28: Hard-x ray flux intensity versus LH power for different phasings (B=2.8 T, Ip=420 kA, $\bar{n}_e = 1.5 \times 10^{13}$ cm^{-3}).

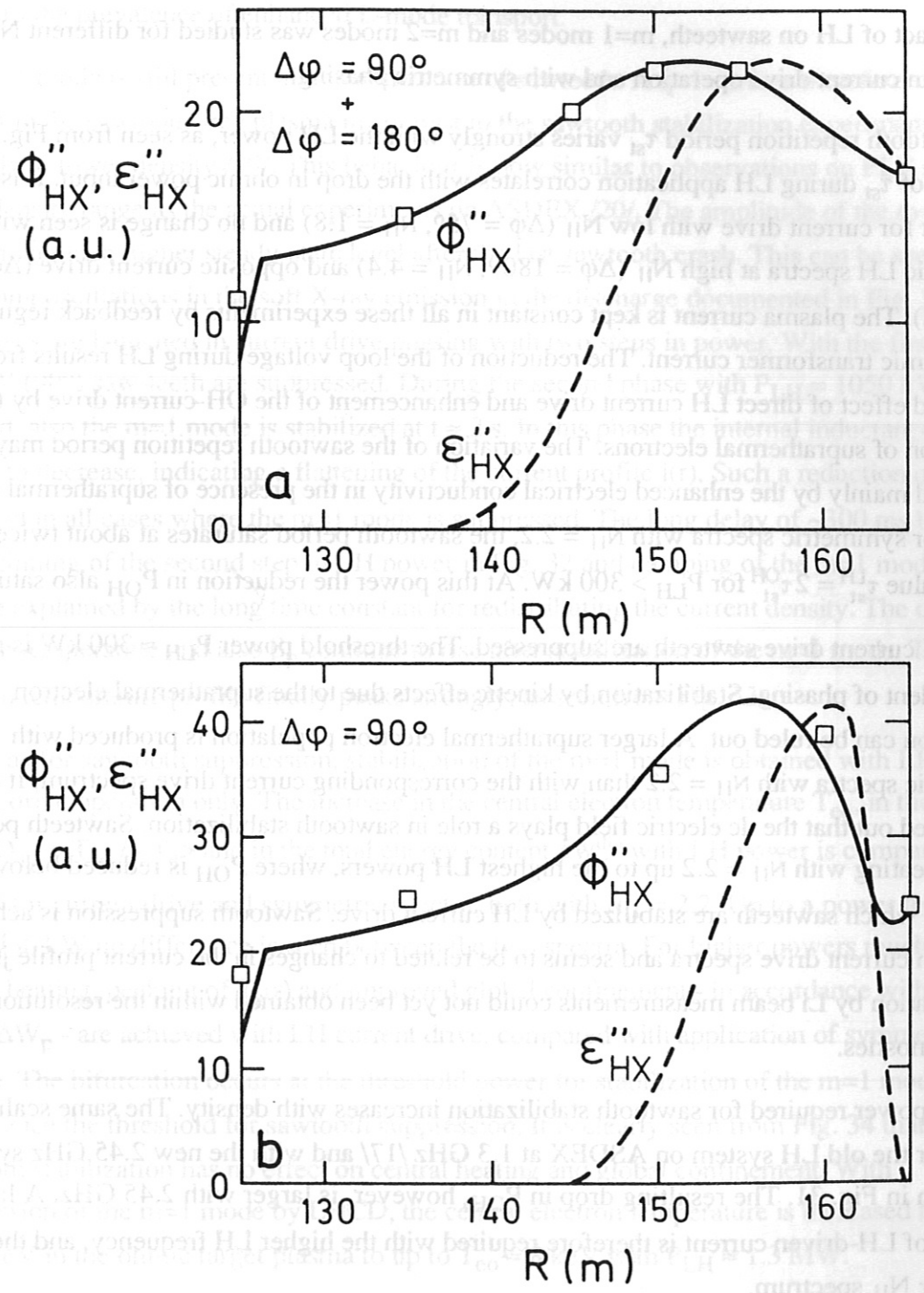

Fig.29: Tangential hard-x ray emission at 100 kev in the backward direction versus tangency major radius (experimental points: open box, fit: full line, calculated radial profile: dotted line; B=2.8 T, Ip=420 kA, $\bar{n}_e$= 1.5 x 10^{13} cm^{-3}).
a: P_{LH}=350+250 KW, $\bar{N}_{||}$=1.8+3.6; b: P_{LH}=1 MW, $\bar{N}_{||}$=1.8.

10. Control of MHD activity

The impact of LH on sawteeth, m=1 modes and m=2 modes was studied for different $N_{||}$ spectra, in current drive operation and with symmetric phasing.

The sawtooth repetition period τ_{st} varies strongly with the LH power, as seen from Fig. 30. The increase of τ_{st} during LH application correlates with the drop in ohmic power input. It is strongest for current drive with low $N_{||}$ ($\Delta\varphi = 75^o$, $\bar{N}_{||} = 1.8$) and no change is seen with symmetric LH spectra at high $N_{||}$ ($\Delta\varphi = 180^o$, $\bar{N}_{||} = 4.4$) and opposite current drive ($\Delta\varphi = -90^o$, $\bar{N}_{||} = 2.2$). The plasma current is kept constant in all these experiments by feedback regulation of the ohmic transformer current. The reduction of the loop voltage during LH results from the combined effect of direct LH current drive and enhancement of the OH-current drive by the generation of suprathermal electrons. The variation of the sawtooth repetition period may be explained mainly by the enhanced electrical conductivity in the presence of suprathermal electrons. For symmetric spectra with $\bar{N}_{||} = 2.2$, the sawtooth period saturates at about twice the ohmic value $\tau_{st}^{LH} = 2\tau_{st}^{OH}$ for $P_{LH} > 300$ kW. At this power the reduction in P_{OH} also saturates.

With LH current drive sawteeth are suppressed. The threshold power $P_{LH} \approx 300$ kW is nearly independent of phasing. Stabilization by kinetic effects due to the suprathermal electron population can be ruled out. A larger suprathermal electron population is produced with symmetric spectra with $\bar{N}_{||} = 2.2$ than with the corresponding current drive spectrum. It can also be ruled out that the dc electric field plays a role in sawtooth stabilization. Sawteeth persist for LH heating with $\bar{N}_{||} = 2.2$ up to the highest LH powers, where P_{OH} is reduced below the values at which sawteeth are stabilized by LH current drive. Sawtooth suppression is achieved only with current drive spectra and seems to be related to changes in the current profile j(r). Confirmation by Li beam measurements could not yet been obtained within the resolution of this diagnostics.

The LH power required for sawtooth stabilization increases with density. The same scaling is found for the old LH system on ASDEX at 1.3 GHz /17/ and with the new 2.45 GHz system as shown in Fig. 31. The resulting drop in P_{OH}, however, is larger with 2.45 GHz. A larger fraction of LH-driven current is therefore required with the higher LH frequency, and the narrower $N_{||}$ spectrum.

Sawtooth suppression does not lead to significant changes in density and temperature profiles at low densities ($\bar{n}_e \leq 2 \cdot 10^{13}$ cm^{-3}). At higher density ($\bar{n}_e \approx 3 \cdot 10^{13}$ cm^{-3}) impurity accumulation may start after stabilization of sawteeth. The central electron temperature then drops and the discharge finally disrupts owing to radiation collapse. In NBI-heated discharges slight peaking of $n_e(r)$ and $T_e(r)$ is obtained after sawtooth suppression by LHCD as already in previous

experiments with 1.3 GHz /18/. No impurity accumulation is encountered in this case, probably owing to the prevalence of enhanced L-mode transport.

The m=1 mode is still present after stabilization of sawteeth. A q=1 surface therefore continues to exist in the sawtooth-free plasma in contrast to the sawtooth stabilization experiments with 1.3 GHz at lower density /19/. This behaviour is now similar to observations on PLT in the same density range as the actual experiments on ASDEX /20/. The amplitude of the m=1 mode grows to a much higher steady-state level after the last sawtooth crash. This can be seen from the strong oscillations in the soft X-ray emission in the discharge documented in Fig. 32. There LH waves are launched in current drive phasing with two steps in power. With the first level of 560 kW (90°) saw-teeth are suppressed. During the second phase with P_{LH} = 1050 kW injected, also the m=1 mode is stabilized at t ≈ 2 s. In this phase the internal inductance l_i starts slowly to decrease, indicating a flattening of the current profile j(r). Such a reduction of l_i is observed in all cases where the m=1 mode is suppressed. The long delay of ~300 ms between the beginning of the second step in LH power in Fig. 32 and damping of the m=1 mode may then be explained by the long time constant for redistributing the current density. The central electron temperature and also β_p continue to rise after stabilization of the m=1 mode. The electron temperature profile finally peaks strongly, as seen from Fig. 33.

Again, as for sawtooth suppression, stabilization of the m=1 mode is obtained with LH in current drive operation only. The increase in the central electron temperature T_{eo}, in the peaking factor $Q_{T_e} = T_{eo} / \langle T_e \rangle$ and in the total energy content ΔW_p^{dia} with LH power is compared in Fig. 34 for current drive and symmetric spectra, both with $\bar{N}_{||} = 2.2$. Up to a power level of $P_{tot} \approx 750$ kW no difference is seen between the two spectra. For higher powers much stronger central heating, peaking of $T_e(r)$ and improved global confinement - in accordance with the larger ΔW_p - are achieved with LH current drive, compared with application of symmetric LH spectra. The bifurcation occurs at the threshold power for stabilization of the m=1 mode.This is about twice the threshold for sawtooth suppression. It is clearly seen from Fig. 34 that sawtooth stabilization has no effect on central heating and global confinement. With suppression of the m=1 mode by LHCD, the central electron temperature is increased from T_{eo} ≈ 1.8 keV in the ohmic target plasma to up to $T_{eo} \approx 8$ keV with $P_{LH} \approx 1.3$ MW.

While the electron temperature profile peaks strongly up to values of $Q_{T_e} \approx 5$, the current profile j(r) flattens. Current and temperature profiles can therefore be completely decoupled with LH current drive, as already shown in previous LH experiments with 1.3 GHz on ASDEX.

Stabilization of the m=1 mode could also be achieved with LH current drive during NBI. Peaking of $T_e(r)$ and enhanced global confinement were also obtained in this case.

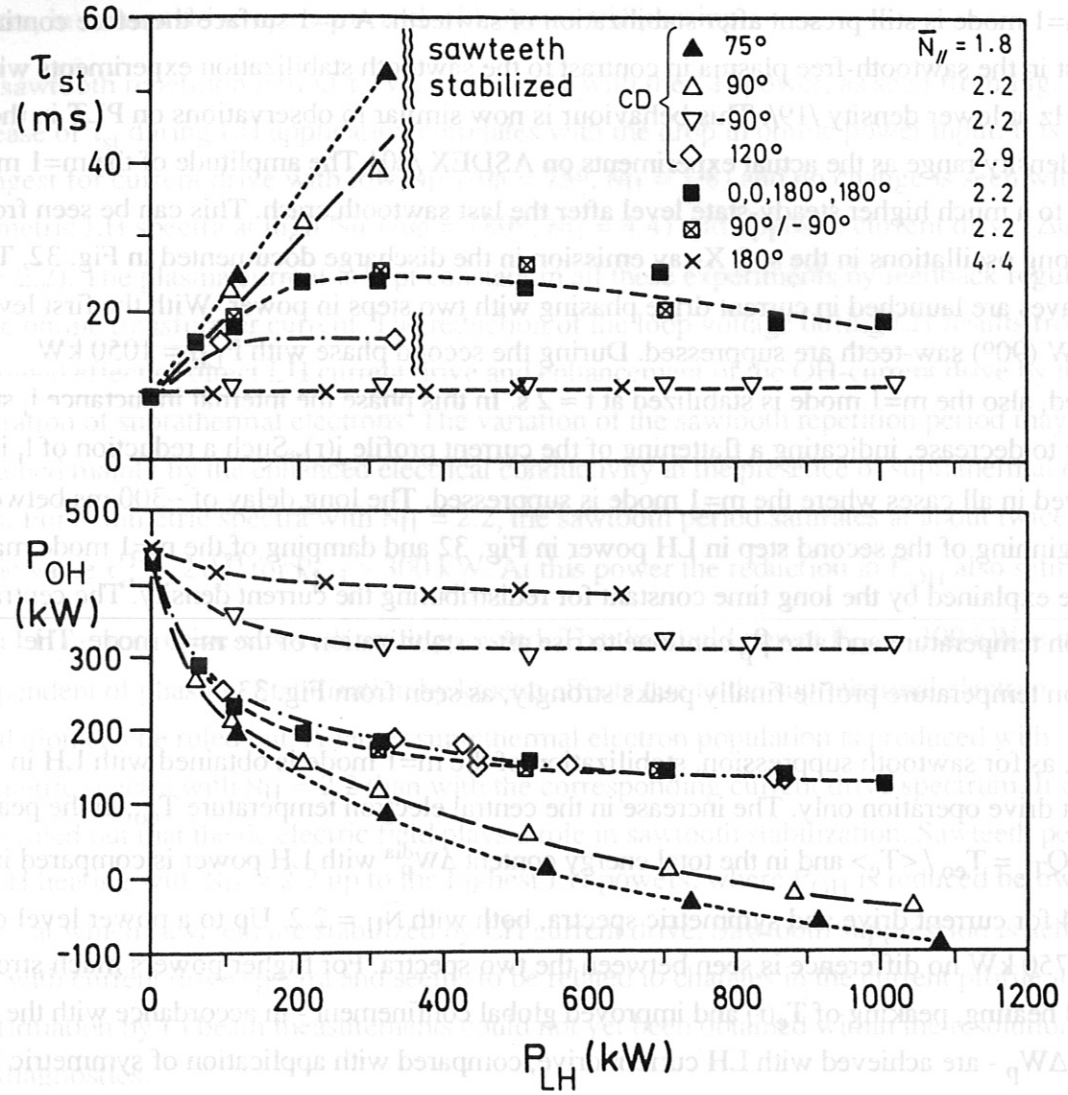

Fig. 30: Variation of sawtooth period and residual ohmic power input with LH power for different $N_{||}$ spectra. $B_t = 2.8$ T, $I_p = 420$ kA, $\bar{n}_e = 1.4 \cdot 10^{13}$cm^{-3}.

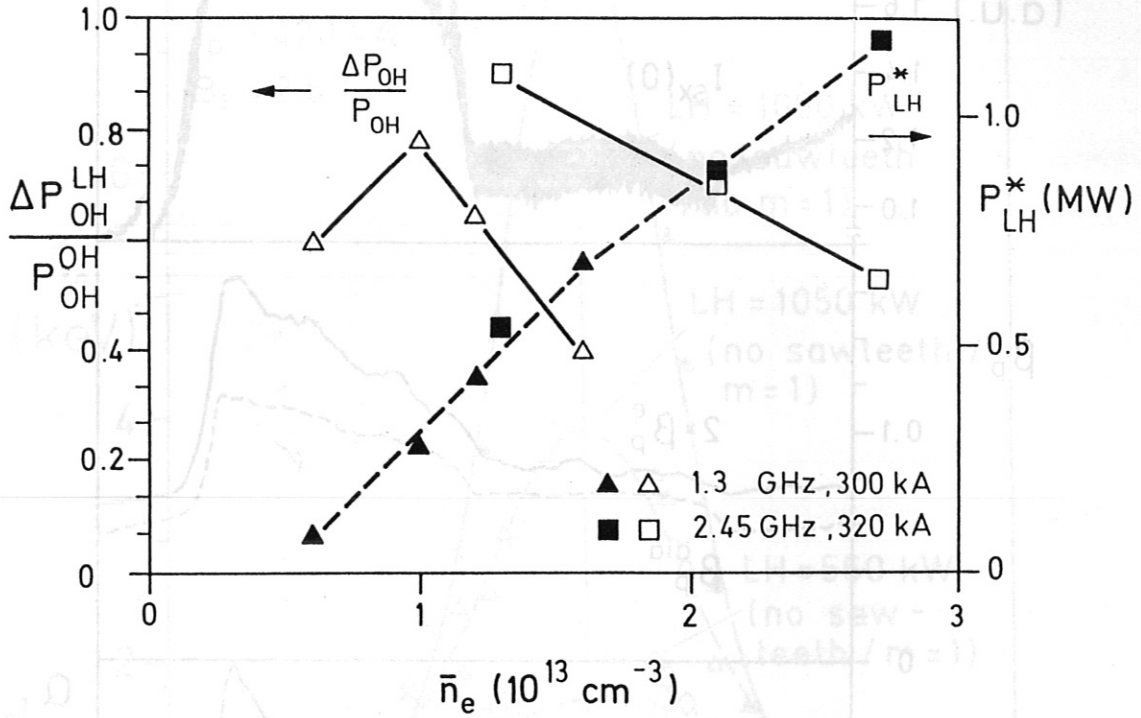

Fig. 31: Variation of the threshold LH power P^*_{LH} for sawtooth stabilization and the corresponding drop in ohmic power input $\Delta P^{LH}_{OH} / P^{OH}_{OH}$ with density, for the two LH systems at 1.3 and 2.45 GHz on ASDEX.

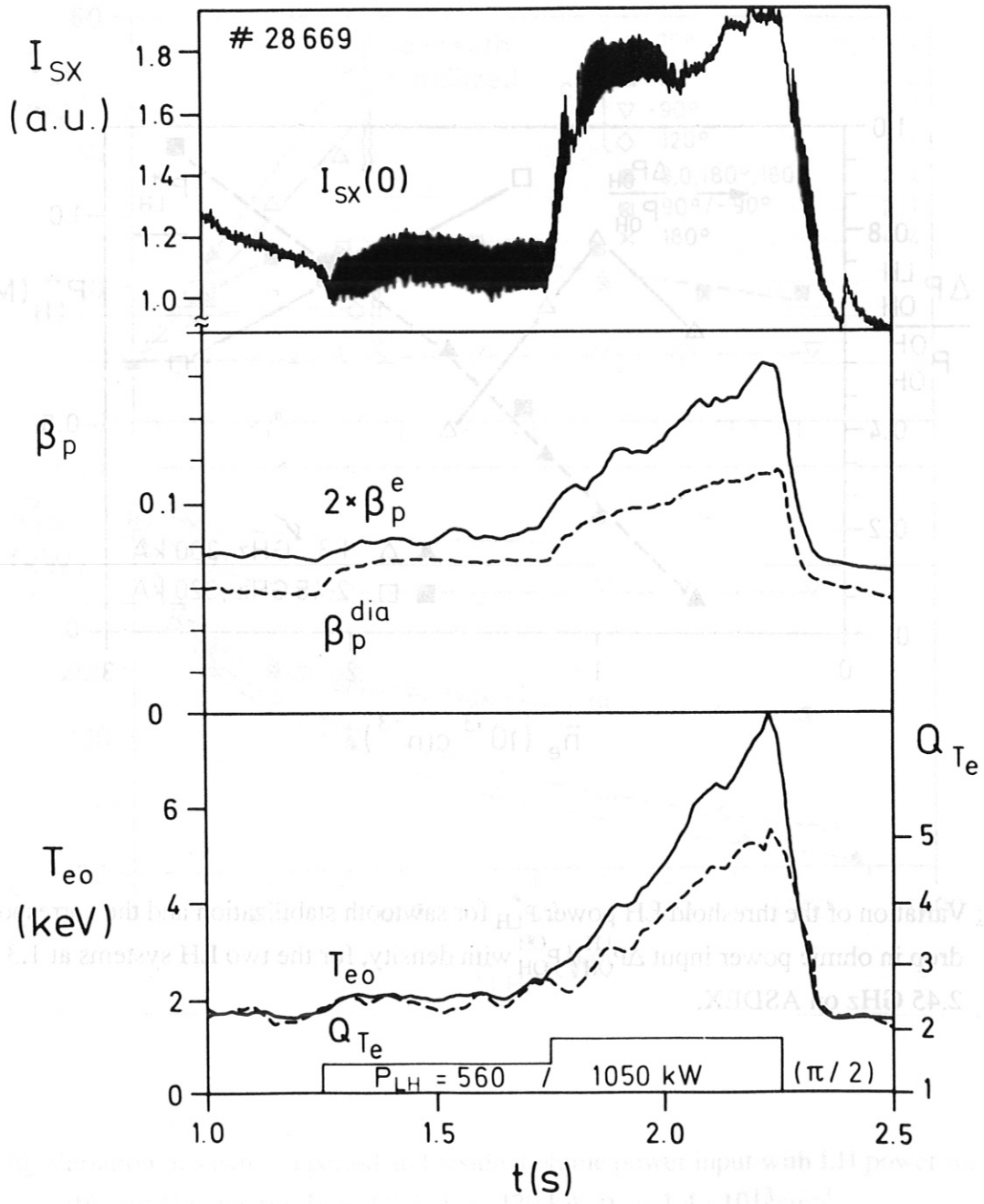

Fig. 32: Temporal evolution of plasma parameters in a discharge with stabilization of sawteeth by LHCD in a first power step at 560 kW and stabilization of the m=1 mode with a second step at 1050 kW. B_t = 2.8 T, I_p = 420 kA, LHCD with π/2, $\overline{N}_{||}$ = 2.2.

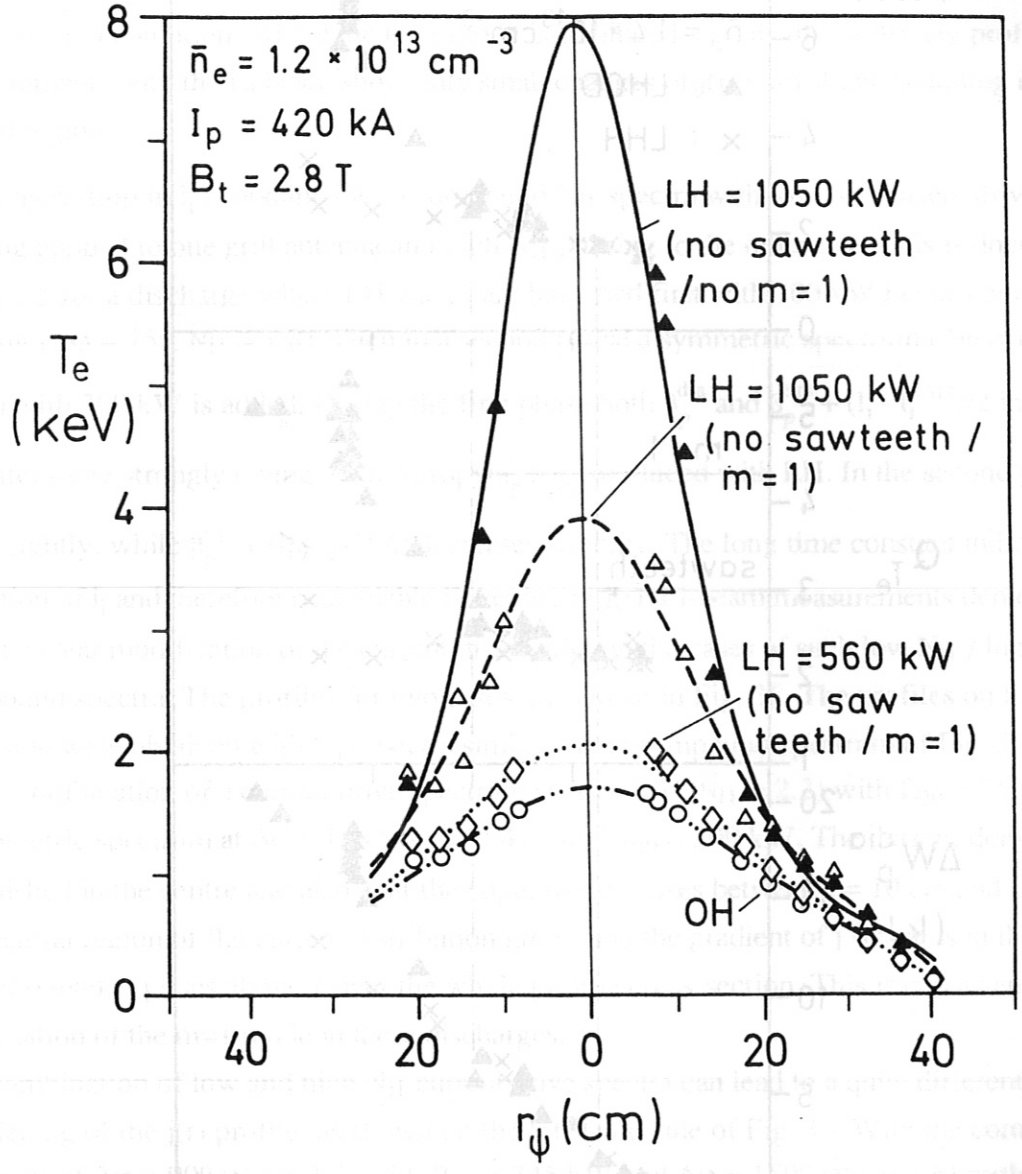

Fig. 33: Radial electron temperature profiles during the different phases of the discharge # 28669 shown in Fig. 24.

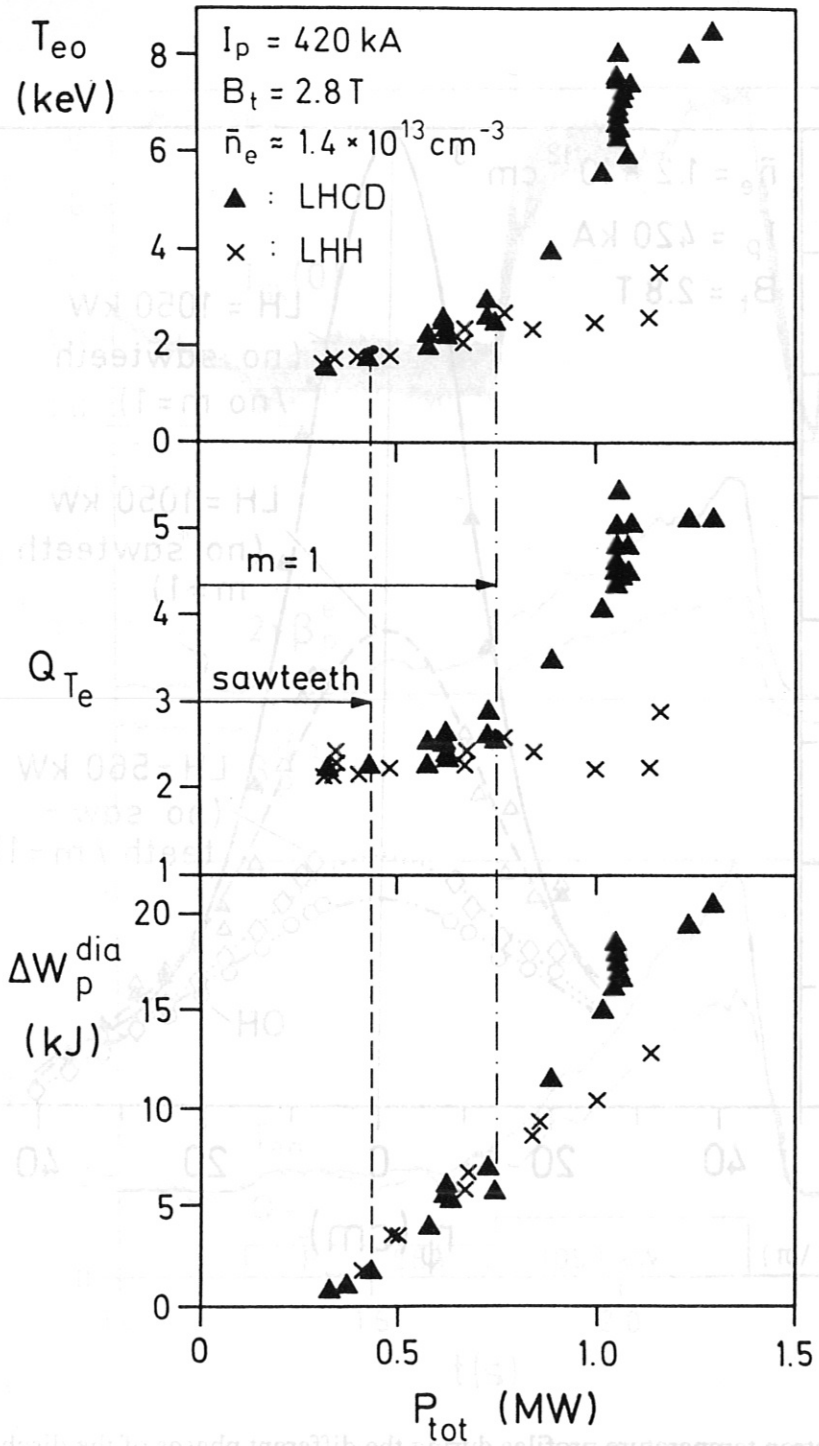

Fig. 34: Variation of central electron temperature T_{eo}, peaking factor $Q_{T_e} = T_{eo} / \langle T_e \rangle$ and increment in energy content, ΔW_p^{dia} with total power input $P_{tot} = P_{OH} + P_{LH}$ for LH current drive (LHCD) and symmetric LH spectra (LHH).

11. Profile control

Optimization of plasma profiles requires control of the local power deposition profile, both in LH current drive and in heating mode /21/. With low $N_{||}$ current drive spectra a reduction of l_i is observed in conditions where the m=1 mode is stabilized. Local current density profile measurements with the Li beam show only small changes of j(r) with slight flattening in the central region.

The largest drop in l_i is obtained with compound $N_{||}$ spectra with low $N_{||}$ current drive phasing applied to one grill antenna and high $N_{||}$ phasing to the other one. This is documented in Fig. 35 for a discharge where LH waves are launched first with 700 kW in current drive phasing ($\Delta\varphi = 75^o$, $\bar{N}_{||} = 1.8$). Then in a second phase a symmetric spectrum ($\Delta\varphi = 180^o$, $\bar{N}_{||} = 4.4$) with 300 kW is added. During the first phase both β_p^{dia} and $\beta_p^{equ} + (l_i - l_i^{OH})/2$ increase, the latter more strongly owing to anisotropy $\beta_p^{||} > \beta_p^{\perp}$ produced with LH. In the second phase β_p^{dia} rises slightly, while $\beta_p^{equ} + (l_i - l_i^{OH})/2$ decreases strongly. The long time constant indicates a reduction of l_i and therefore appreciable flattening of j(r). Li-beam measurements demonstrate in fact a clear modification of the current distribution in the cases of such low $N_{||}$ / high $N_{||}$ compound spectra. The profiles for two cases are shown in Fig. 36. The profiles on the right-hand side were obtained with $N_{||}$ spectra similar to the compound spectrum of Fig. 35, namely with a combination of a current drive spectrum at $\Delta\varphi = 90^o$ ($\bar{N}_{||} = 2.2$) with $P_{90} = 750$ kW and a symmetric spectrum at $\Delta\varphi = 180^o$ ($\bar{N}_{||} = 4.4$) with $P_{180} = 300$ kW. The current density j is diminished in the centre and also near the edge, while it rises between r = 10 cm and r = 20 cm. The central region of flat current distribution grows and the gradient of j steepens in the region further outside. q rises above 1 over the whole plasma cross-section. This is consistent with the stabilization of the m=1 mode in these discharges.

The combination of low and high $N_{||}$ current drive spectra can lead to a quite different kind of broadening of the j(r) profile, as shown on the left-hand side of Fig. 36. With the compound spectrum of $\Delta\varphi = 90^o$ ($\bar{N}_{||} = 2.2$) with $P_{90} = 345$ kW and $\Delta\varphi = 150^o$ ($\bar{N}_{||} = 3.6$) with $P_{150} =$ 260 kW the current density j strongly drops in the centre but this time it rises near the edge. The extension of the central region with flat j(r) distribution remains unchanged and the gradient of j decreases everywhere. q rises above 1 over the whole plasma in this case, as well.

With the injection of compound $N_{||}$ spectra the shape of the current profile can therefore be varied to a large extent. The versatile combination of low and high $N_{||}$ spectral components offers a powerful scheme of minimizing the total LH power required and optimizing local deposition. The high current drive efficiency of low $N_{||}$ waves can be maintained while their deposition is steered by a small amount of power at high $N_{||}$. Similar experiments with

compound $N_{||}$ spectra had been carried out already with the previous 1.3 GHz system /22,23/. But in that case only one single grill antenna with smaller number of waveguides and correspondingly broader $N_{||}$ spectrum was at disposal. Variation of the shape of the $N_{||}$ spectrum was then obtained by varying the power distribution in the individual waveguides. The maximum LH power available in those experiments was therefore limited to low levels comparable with the maximum ohmic power input. The improvement in the flexibility of the spectrum adjustement and the increase in power for profile control at higher density were the main reasons for the installation of the new LH system at 2.45 GHz on ASDEX.

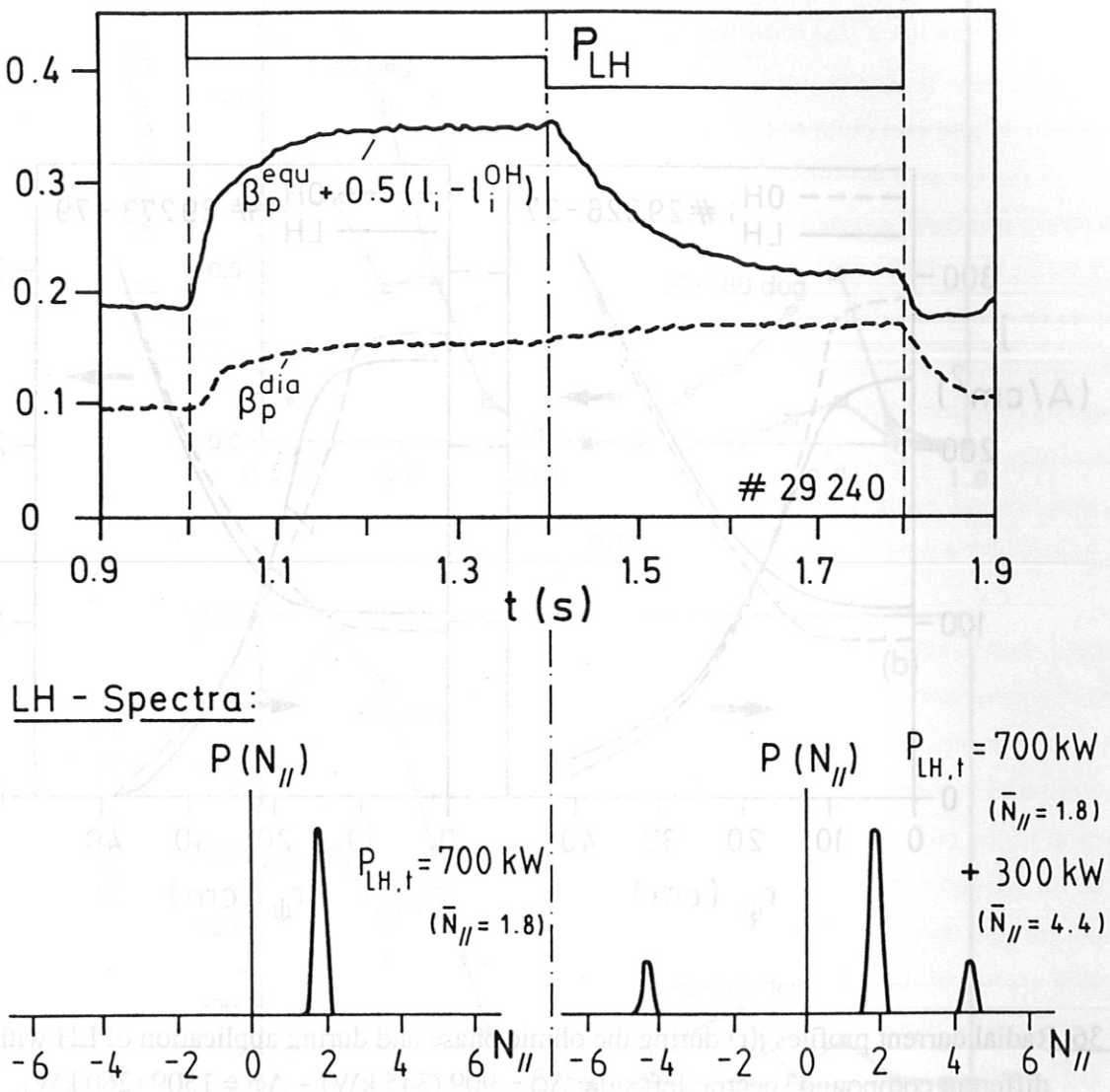

Fig. 35: Temporal evolution of the diamagnetic beta β_p^{dia} and the sum of equilibrium beta and change of the internal inductance, $\beta_p^{equ} + (l_i - l_i^{OH})/2$, during injection of a narrow current drive spectrum and a compound spectrum.

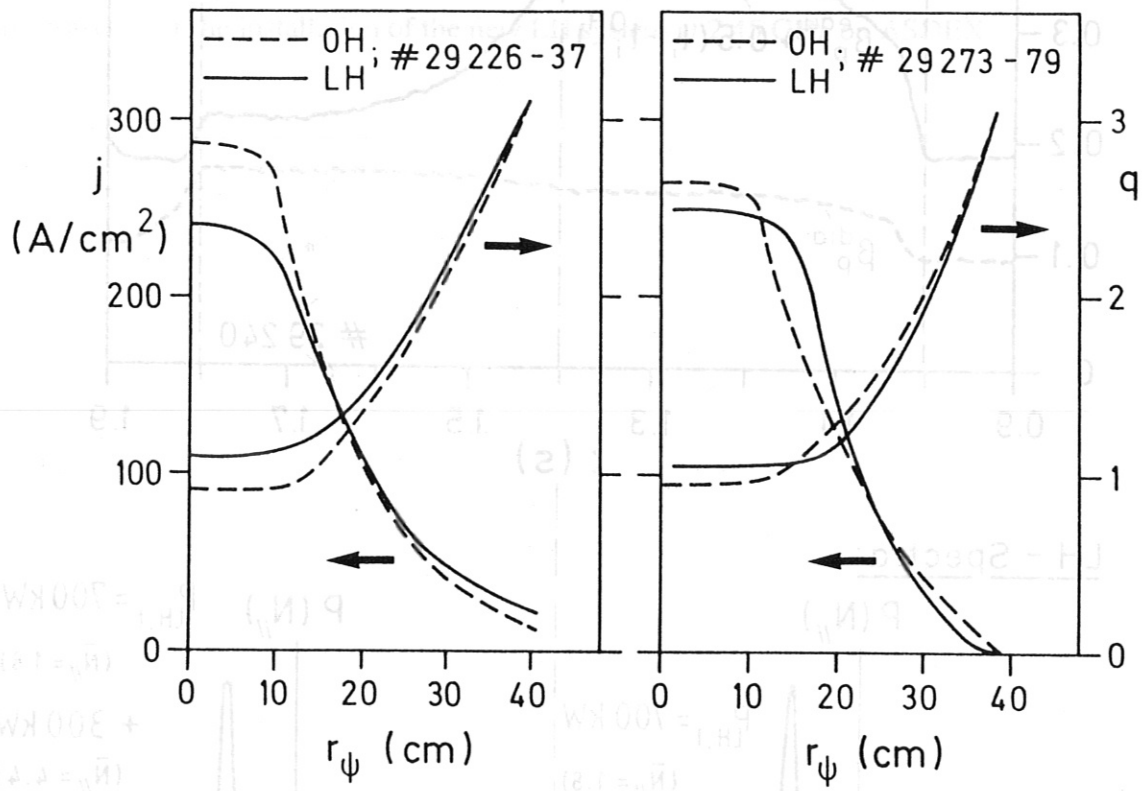

Fig. 36: Radial current profiles j(r) during the ohmic phase and during application of LH with different compound spectra: left side: $\Delta\varphi = 90^o$ (345 kW) + $\Delta\varphi = 150^o$ (260 kW), right side: $\Delta\varphi = 90^o$ (750 kW) + $\Delta\varphi = 180^o$ (300 kW). $B_t = 2.8$ T, $I_p = 420$ kA, $\bar{n}_e = 1.35 \cdot 10^{13}$ cm^{-3}.

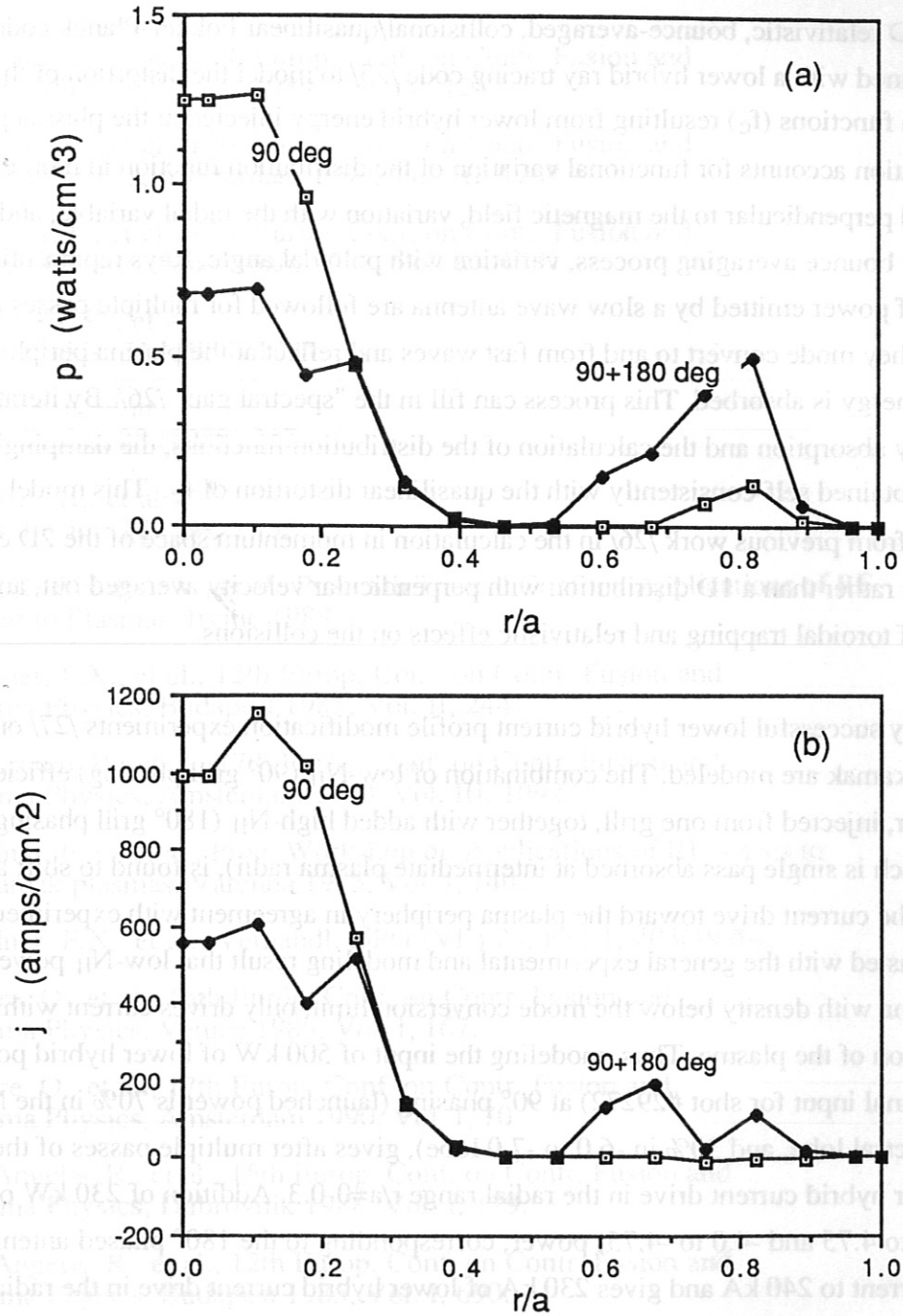

Fig. 37: Radial profiles of (a) absorbed power density, and (b) rf driven current for the 90° and 90°+180° phasing cases.

12.Fokker-Planck Modelling of current profile modification

The CQL3D relativistic, bounce-averaged, collisional/quasilinear Fokker-Planck code /24/ has been combined with a lower hybrid ray tracing code /25/ to model the distortion of the electron distribution functions (f_e) resulting from lower hybrid energy injected at the plasma periphery. The calculation accounts for functional variation of the distribution function in momentum space parallel and perpendicular to the magnetic field, variation with the radial variable, and, implicitly through the bounce averaging process, variation with poloidal angle. Rays representing the spectrum of power emitted by a slow wave antenna are followed for multiple passes across the plasma as they mode convert to and from fast waves and reflect at the plasma periphery, until the wave energy is absorbed. This process can fill in the "spectral gap" /26/. By iterating between ray absorption and the calculation of the distribution functions, the damping of the ray energy is obtained self-consistently with the quasilinear distortion of f_e. This model differs essentially from previous work /26/ in the calculation in momentum space of the 2D electron distribution rather than a 1D distribution with perpendicular velocity averaged out, and by inclusion of toroidal trapping and relativistic effects on the collisions.

Recent, very successful lower hybrid current profile modification experiments /27/ on the ASDEX tokamak are modeled. The combination of low-$N_{||}$ (90° grill phasing) efficient current drive power, injected from one grill, together with added high-$N_{||}$ (180° grill phasing) heating power (which is single pass absorbed at intermediate plasma radii), is found to shift a substantial portion of the current drive toward the plasma periphery in agreement with experiment. This is to be contrasted with the general experimental and modeling result that low-$N_{||}$ power injected into a plasma with density below the mode conversion limit, only drives current within the central region of the plasma. Thus, modeling the input of 500 kW of lower hybrid power (75% of the nominal input for shot #29272) at 90° phasing (launched power is 70% in the $N_{||}$= 1.85 to 2.55 spectral lobe, and 30% in -6.0 to -7.0 lobe), gives after multiple passes of the rays, 365 kA of lower hybrid current drive in the radial range r/a=0-0.3. Addition of 230 kW of high-$N_{||}$ ($N_{||}$ = 4.5 to 4.75 and -4.0 to -4.75) power, corresponding to the 180° phased antenna, reduces the core current to 240 kA and gives 230 kA of lower hybrid current drive in the radial range r/a=0.6-0.9. The steady state internal inductance resulting from these two simulations is 1.7 and 0.7, respectively. Corresponding power deposition and current drive profiles are shown in Figure 37(a) and 37(b). The mechanism for the current profile broadening is that the single pass absorption the high-$N_{||}$ spectra enhances the tail electron distribution within the radial range r/a=0.6-0.9 to the extent that a significant portion of the low-$N_{||}$ spectrum is absorbed at that location.

References

/1/ Leuterer, F., et al., 16th Europ. Conf. on Contr. Fusion and Plasma Physics, Venice 1989, Vol. IV, 1287.

/2/ Leuterer, F., et al., 17th Europ. Conf. on Contr. Fusion and Plasma Physics, Amsterdam 1990, Vol. III, 1287.

/3/ Leuterer, F., et al., 17th Europ. Conf. on Contr. Fusion and Plasma Physics, Amsterdam 1990, Vol. III, 1291.

/4/ Yoshioka, K., et al., Phys. Fluids. 31 (1988) 1224.

/5/ Stevens, J., et al. Nucl. Fusion 28 (1988) 217.

/6/ Cesario, R., et al., Nucl. Fusion 27 (1987) 435.

/7/ Pericoli-Ridolfini,V., et al., Proc. 8th Topical Conf. on Applications of RF Power to Plasmas, Irvine 1988.

/8/ Söldner, F.X., et al., 12th Europ. Conf. on Contr. Fusion and Plasma Physics, Budapest 1985, Vol. II, 244.

/9/ Bartiromo, R., et al., 17th Europ. Conf. on Contr. Fusion and Plasma Physics, Amsterdam 1990, Vol. III, 1092.

/10/ Söldner, F.X., et al., Proc. Workshop on Applications of RF waves to Tokamak plasmas, Varenna 1985, Vol. I, 740.

/11/ Söldner, F.X., et al., Verhandl. DPG (VI) 25, P11.1, 403(1990).

/12/ Gehre, O., et al., 16th Europ. Conf. on Contr. Fusion and Plasma Physics, Venice 1989, Vol. I, 167.

/13/ Gehre, O., et al., 17th Europ. Conf. on Contr. Fusion and Plasma Physics, Amsterdam 1990, Vol. I, 70.

/14/ De Angelis, R., et al., 15th Europ. Conf. on Contr. Fusion and Plasma Physics, Dubrovnik 1988, Vol. I, 179.

/15/ De Angelis, R., et al., 12th Europ. Conf. on Contr. Fusion and Plasma Physics, Budapest 1985, Vol. I, 690.

/16/ Bartiromo, R., et al., Nucl. Fusion 26 (1986) 1106.

/17/ Söldner, F.X., et al., Phys. Rev. Lett. 57 (1986), 1137.

/18/ Söldner, F.X., et al., 13th Europ. Conf. on Contr. Fusion and Plasma Physics, Schliersee 1986, Vol. II, 319.

/19/ McCormick, K., et al., Phys. Rev. Lett. 58 (1987), 491.

/20/ Chu, T.K., et al., Nucl. Fusion 26 (1986) 666.

/21/ Söldner, F.X., et al., Proc. 7th Topical. Conf. on Applications of RF Power to Plasmas, Kissimmee 1986, 102.

/22/ Leuterer, F., et al., 13th Europ. Conf. on Contr. Fusion and Plasma Physics, Schliersee 1986, Vol. II, 409.

/23/ Söldner, F.X., et al., 14th Europ. Conf. on Contr. Fusion and Plasma Physics, Madrid 1987, Vol. II, 831.

/24/ Kerbel, G.D. and M.G. McCoy, Phys. Fluids 28, 3629 (1985); M.G. McCoy, G.D. Kerbel, and R.W. Harvey, AIP Conf. Proc. 159, 77 (1987); R.W. Harvey, M.G. McCoy, and G.D. Kerbel, ibid., 49.

/25/ Brambilla,M., Comput. Phys. Rep. 4, 71 (1986).

/26/ Bonoli, P.T. and R.C. Englade, Phys. Fluids 29, 2937 (1986).

/27/ Söldner, F.X., et al., 17th Europ. Conf. on Contr. Fusion and Plasma Physics, Amsterdam 1990, Vol. III, 1323.